

# Tuning current flow in superconducting thin film strips by control wires. Applications to single photon detectors and diodes.

Alex Gurevich\*

Department of Physics, Old Dominion University, Norfolk, Virginia 23529, USA.

(Dated: February 4, 2026)

It is shown that integration of a thin film superconducting strip with current-carrying control wires enables one to engineer a profile of supercurrent density  $J(x)$  with no current crowding at the edges of a strip wider than the magnetic Pearl length  $\Lambda$ . Moreover,  $J(x)$  in a strip can be tuned by control wires to produce an inverted  $J(x)$  profile with dips at the edges to mitigate current crowding at lithographic defects and block premature penetration of vortices. These conclusions are corroborated by calculations of  $J(x)$  in a thin strip coupled inductively with side control wires or in bilayer strip structures by solving the London and Ginzburg Landau equations in the thin film Pearl limit. Thermally-activated penetration of vortices from the edges and unbinding of vortex-antivortex pairs in inverted  $J(x)$  profiles are evaluated. It is shown that these structures can be used to develop single-photon strip detectors much wider than  $\Lambda$ . Such detectors can be tuned *in situ* by varying current in control wires to reach the ultimate photon sensitivity limited by unbinding of vortex-antivortex pairs. The structures considered here also exhibit a non-reciprocal current response and behave as superconducting diodes.

## I. INTRODUCTION

Thin superconducting films and micro resonators are instrumental in superconducting electronics<sup>1,2</sup>. Particularly, superconducting nanowire single-photon detectors (SNSPD) <sup>3-5</sup> with up to ps time resolution have proliferated in quantum information technology<sup>6-14</sup>, astronomy<sup>15</sup>, high energy particle detectors and search for dark matter<sup>16-18</sup>, or deep brain imaging<sup>19-21</sup>. One of the goals of the SNSPD technology is the development of large-area detector arrays with a nearly 100 % photon sensitivity into infrared light <sup>4,5,21</sup>. Such detectors are photon-sensitive at bios currents  $I_i < I_s < I_b$ , where the onset current  $I_i$  and the switching current  $I_b$  are fractions of the depairing current  $I_d$ .

Boosting the sensitivity of SNSPD requires increasing both the operational current range  $I_b - I_i$  and the detector area. As the bios current  $I$  approaches  $I_d$ , the photon energy required to form a critical hotspot expanding across the strip decreases and the minimum detectable photon energy becomes weakly dependent on the strip width <sup>22</sup> so it may be beneficial to push  $I_b$  toward  $I_d$  as much as possible. However, there are limitations of how close  $I_b$  can approach  $I_d$  and how much the width of a straight strip be increased. First, thin strips inevitably have lithographic defects causing localized current crowding along the edges <sup>23,24</sup>. For instance, a semi-circular edge indentation of radius larger than the coherence length  $\xi$  causes a two-fold local increase in the sheet current density  $J(x)$ , while a sharp indentation or microcrack causes even greater current crowding which can initiate vortex jets <sup>25-28</sup> or dendritic thermo-magnetic vortex avalanches <sup>29-31</sup> destroying the non-dissipative current-carrying state. Second, the Meissner effect causes current crowding at the edges which becomes detrimental for the SNSPD performance as the width of the strip exceeds the magnetic Pearl length  $\Lambda$  <sup>32,33</sup>. Interplay of these effects illustrated in Fig. 1 decreases the entry energy barrier

of vortices, greatly increasing the dark count rate due to thermally-activated penetration of vortices from the edges at currents well below  $I_d$ . To increase the photon-sensitive detector area, meandering SNSPDs structures have been developed <sup>3-5</sup>. To mitigate the current crowding by the edge roughness, the active SNSPD areas have been irradiated with heavy ions leaving intact the long edges along the strip <sup>34</sup> and the bend regions <sup>35</sup>.

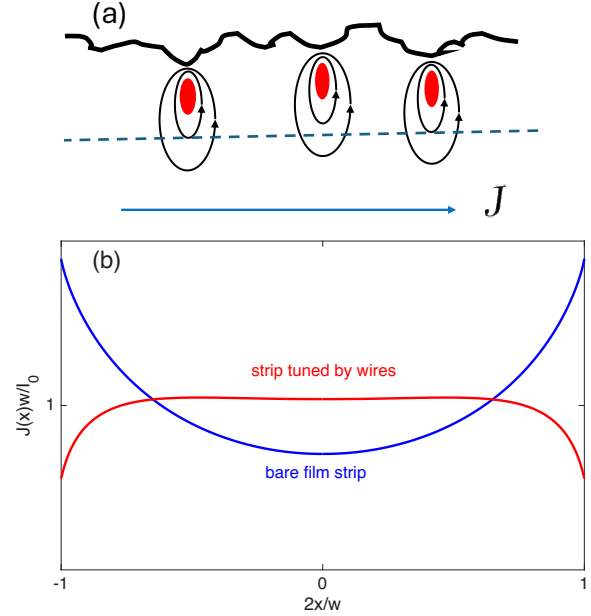


FIG. 1. Factors limiting the maximum current in superconducting thin strips: (a) edge roughness causing local current crowding and premature penetration of vortices. The dashed line depicts a boundary of a layer in which local variations of current density are essential. (b) The Pearl current crowding at the edges of a bare strip (blue). An inverted current density profile  $J(x)$  in a strip tuned by control wires (red) deactivating both the edge defects and the Pearl current crowding.

This work explores boosting the SNSPD performance by forming an inverted profile of  $J(x)$  in a superconducting strip shown in Fig. 1. Here a reduced current density at the edges mitigates the effect of current crowding defects and eliminates current crowding caused by the Pearl screening. It is shown that such  $J(x)$  profile can indeed be produced and *tuned in situ* in a superconducting strip coupled inductively with adjacent current-carrying wires or other thin film structures. These control wires produce the magnetic field that counters the perpendicular component of the self field of SNSPD and redistribute  $J(x)$  in the strip as shown in Fig. 1. Such structures can provide a flat portion of  $J(x)$  in the photon-sensitive area of the strip and controllable dips at the edges which block premature penetration of vortices and give rise to a non-reciprocal current-voltage characteristic of a superconducting diode. Furthermore, currents in the control wires can be tuned in such a way that the SNSPD reaches the ultimate performance limit determined by the unbinding of vortex-antivortices pairs in the strip<sup>36,37</sup>. Such device architecture lifts the SNSPD size limitations and opens opportunities for the development of straight strip detectors much wider than the Pearl length. This approach has been recently implemented in Ref. 38 which reported the development of 3 nm thick and up to 0.1 mm wide WSi strip detectors integrated with Nb side wires ("rails"), reaching 100% sensitivity into infrared, up to 20 % larger switching currents and the dark count rate decreased by up to 8 orders of magnitude. Manipulation of resistive switching in superconducting films by current-carrying control wires has a long history which goes back to the development of cryotrons<sup>39-41</sup>.

The paper is organized as follows. In Sec. II the sheet current density  $J(x)$  in a thin film strip coupled with control wires is calculated by solving the London equations. It is shown that the inverted profile of  $J(x)$  can be produced in strips of any width even much wider than the Pearl length. In Sec. III bilayers structures are considered in which one of the layers is used to tune  $J(x)$  in the prime strip. In Sec. IV the nonlinear pairbreaking effects in a bare strip and a strip with control wires are considered by solving the Ginzburg-Landau (GL) equations for  $J(x)$ . It is shown that the strip inductively coupled with control wires has a non-reciprocal current response and can behave as a tunable superconducting diode. In Sec. V the dynamics of vortices driven by the inverted profile  $J(x)$  is considered. The dark counts caused by penetration of vortices through the edges and unbinding of vortex-antivortex pairs in the strip are evaluated. Sec. VI concludes with discussions of the results.

## II. FIELD AND CURRENT IN A STRIP BETWEEN CONTROL WIRES

Consider a long thin strip of width  $w$  in the plane  $y = 0$  between two control strip wires of width  $l$  at  $w/2 + b < x < w/2 + b + l$  and  $-w/2 - b - l < x < -w/2 - b$ , as

shown in Fig. 2. Each control wire is raised by  $h$  and spaced by  $b$  from the edge of the central strip. Here the central strip carries a dc current  $I$  and each control wire carries a dc current  $I_1$ , all strips are infinite along  $z$  and no external magnetic field is applied.

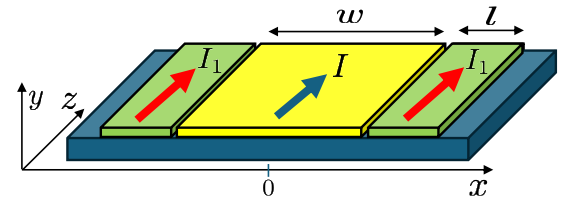


FIG. 2. A strip of width  $w$  between two control strip wires of width  $l$ . The coordinate axes are shifted downward for clarity.

In this paper thin films of thickness  $d$  much smaller than the London penetration depth  $\lambda$  are considered. In this case the magnetic field  $B_z$  along the strips vanishes and  $B_x = \partial A / \partial y$  and  $B_y = -\partial A / \partial x$  are expressed in terms of the vector potential  $\mathbf{A}(x, y) = [0, 0, A(x, y)]$  caused by currents flowing along  $z$ . In this thin film Pearl limit,  $A(x, y)$  satisfies the London equation<sup>32,33</sup>:

$$\lambda^2 \nabla^2 A - dQ(x)\delta(y) = 0, \quad (1)$$

where the gauge-invariant  $\mathbf{Q} = \mathbf{A} + (\phi_0/2\pi)\nabla\theta$  is proportional to the supercurrent density  $\mathbf{j} = -\mathbf{Q}/\mu_0\lambda^2$  in the film,  $\theta$  is the phase of the superconducting order parameter and  $\phi_0$  is the magnetic flux quantum. In this planar geometry  $j_x = j_y = 0$  and  $j_z(x)$  flowing along the strips can depend only on  $x$  so the phase gradient  $\nabla\theta = (0, 0, \theta')$  has only a constant z-component  $\theta'$  independent of  $x$ . The solution of Eq. (1) describing current flow in the absence of vortices is given by:

$$A(x, y) = \frac{dw}{8\pi\lambda^2} \int_{-1}^1 \ln[(x-u)^2 + y^2]Q(u)du + \quad (2)$$

$$\frac{d_1 w}{8\pi\lambda_1^2} \left[ \int_{1+b}^{1+b+l} \ln[(x-u)^2 + (y-h)^2]Q_1(u)du + \quad (3) \right.$$

$$\left. \int_{-1-b-l}^{-1-b} \ln[(x-u)^2 + (y-h)^2]Q_2(u)du \right].$$

Here  $Q(x)$ ,  $Q_1(x)$  and  $Q_2(x)$  describe superflow in the strip, the right and the left control wires, respectively,  $\lambda$  and  $\lambda_1$  are the London penetration depths in the strip and the control wire,  $d$  and  $d_1$  are their respective thicknesses, and all lengths are in units of  $w/2$ . If both control wires carry equal parallel currents, the symmetries  $Q(u) = Q(-u)$  and  $Q_1(u) = Q_2(-u)$  reduce Eq. (2) to:

$$A(x, y) = k \int_0^1 \ln[(u^2 - x^2 + y^2)^2 + 4x^2y^2]Q(u)du + \quad (4)$$

$$k_1 \int_{1+b}^{1+b+l} \ln[(x^2 - u^2)^2 + 2(y-h)^2(x^2 + u^2) + (y-h)^4]Q_1(u)du,$$

where  $k = w/4\pi\Lambda$ ,  $k_1 = w/4\pi\Lambda_1$ , and  $\Lambda = 2\lambda^2/d$  and  $\Lambda_1 = 2\lambda_1^2/d_1$  are the Pearl screening lengths<sup>32</sup> in SNSPD and control wires, respectively.

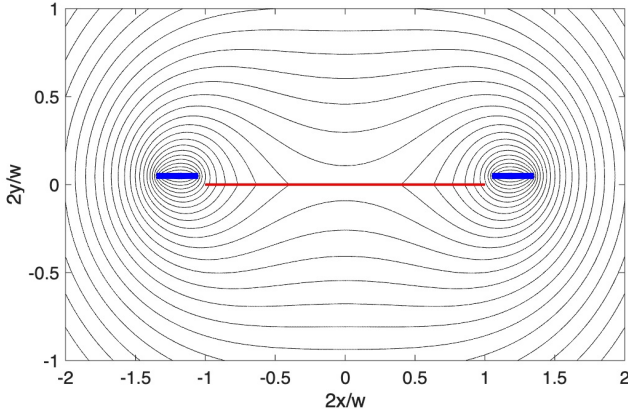


FIG. 3. Magnetic field lines calculated from Eqs. (4) - (6) for  $l = 0.15w$ ,  $k = 0.03$ ,  $k_1 = 50k$ ,  $b = h = 0.05w$ .

Setting  $y = 0$  in Eq. (4) and using  $A(x, 0) = Q(x, 0) - \phi_0\theta'/2\pi$  gives two coupled equations for  $Q(x)$  and  $Q_1(x)$ :

$$Q(x) - 2k \int_0^1 \ln|x^2 - u^2| Q(u) du - \quad (5)$$

$$k_1 \int_{1+b}^{1+l+b} \ln[(u^2 + h^2 - x^2)^2 + 4h^2x^2] Q_1(u) du = \alpha,$$

$$Q_1(x) - 2k_1 \int_{1+b}^{1+b+l} \ln|x^2 - u^2| Q_1(u) du - \quad (6)$$

$$k \int_0^1 \ln[(u^2 + h^2 - x^2)^2 + 4h^2x^2] Q(u) du = \beta,$$

where  $\alpha = \phi_0\theta'_0/2\pi$  and  $\beta = \phi_0\theta'_1/2\pi$  with constant phase gradients  $\theta'_0$  and  $\theta'_1$ . Equations (5) and (6) were solved as described in Appendix A, where  $\alpha$  and  $\beta$  are expressed in terms of currents  $I$  and  $I_1$ . In numerical calculations the material parameters of a 4 nm thick  $\text{W}_{0.8}\text{Si}_{0.2}$  amorphous film with  $T_c = 4.1$  K,  $\lambda = 700$  nm, and  $\Lambda = 245 \mu\text{m}$ <sup>42</sup> at 1K were used. The control wires are assumed to be made of a moderately clean Nb with  $\lambda = 50$  nm,  $\xi = 32$  nm. For these parameters, the ratio  $k_1/k$  varies from 200 to 1000 as  $d_1$  is increased from 4 nm to 20 nm but  $k_1/k$  can be lower for higher concentration of nonmagnetic impurities in Nb. After  $Q(x)$  and  $Q_1(x)$  are obtained,  $\mathbf{H}(x, y)$  around the strip is calculated using Eq. (2). As shown in Fig. 3, the magnetic field of control wires counters the self field of the strip at the edges, mitigating the Pearl current crowding.

Examples of  $J(x)$  in strips of different widths calculated from Eqs. (5) and (6) are shown in Fig. 4. Here the blue lines show  $J(x)$  in a single strip, where  $J(x)$  peaks at the edges due to the Pearl screening in thin films, the peaks increasing as the strip gets wider. Raising the current  $I_1$  in the control wires eliminates the Pearl peaks in  $J(x)$  and produces inverted  $J(x)$  profiles with

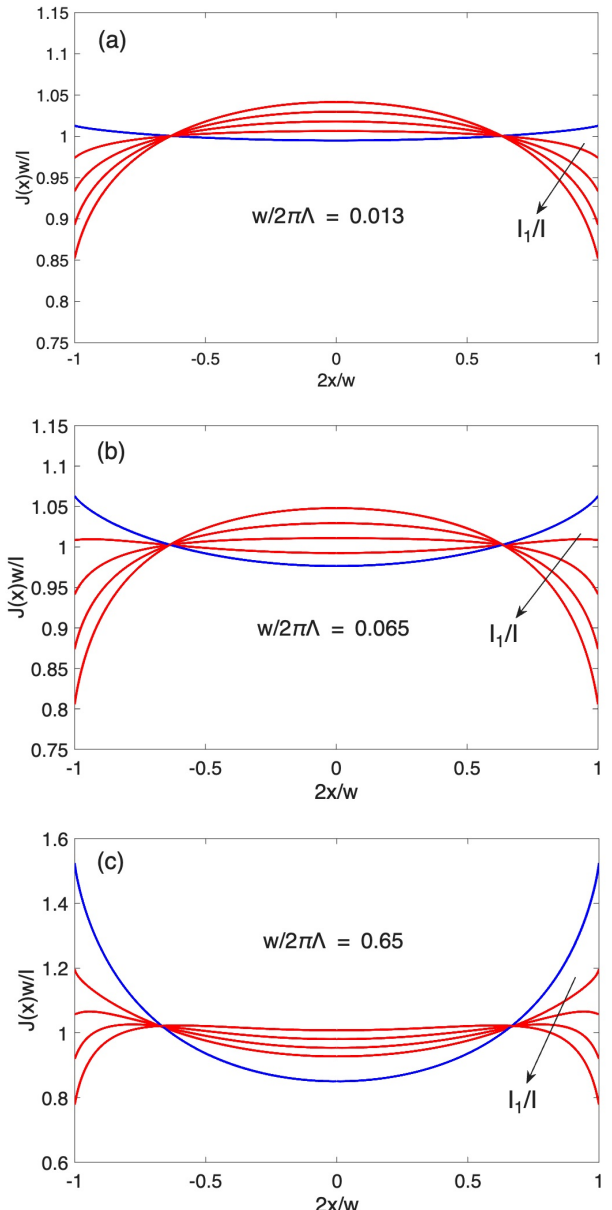


FIG. 4. Sheet current density  $J(x)$  calculated for different strip widths  $w$  and normalized control currents  $I_1/I$  for  $\text{W}_{0.8}\text{Si}_{0.2}$  films with  $d = 4$  nm,  $\Lambda = 245 \mu\text{m}$ <sup>42</sup>,  $k_1 = 200k$  and  $l = 0.15w$ : (a)  $w \approx 20 \mu\text{m}$ ,  $I_1/I = 2.5, 5.03, 7.58, 10.12$ , (b)  $w \approx 100 \mu\text{m}$ ,  $I_1/I = 0.79, 1.62, 2.46, 3.31$ , (c)  $w \approx 1 \text{ mm}$ ,  $I_1/I = 0.64, 0.82, 1.01, 1.21$ .

dips at the edges of the strip. The dips deepen as  $I_1$  is increased at a fixed current  $I$  in the strip. For the above parameters, the dips in  $J(x)$  are produced by currents in the control wires well below the depairing current, while the local  $J(x)$  at the edge or the center of the strip can approach  $J_d$ , as will be shown below. For a narrow strip with  $w < 0.1\Lambda$  represented by Fig. 4a, the self-field effects causing the Pearl current crowding are very weak, so the control current  $I_1$  is to be large enough  $\simeq (2 - 10)I$

to push the current density in the strip away from the edges. As the width increases, the dips in  $J(x)$  at the edges can be produced by smaller control current relative to  $I$ . Shown in Fig. 4c is  $J(x)$  in a strip 4 times wider than  $\Lambda$ . Here  $J(x)$  is nearly flat in the most part of the strip with narrow dips at the edges.

These results show that tuning  $J(x)$  in the strip by increasing the control current eliminates the Pearl current crowding in a strip of any width while producing controllable dips in  $J(x)$  at the edges. The latter deactivate the lithographic defects depicted in Fig. 1a by reducing  $J(\pm w/2)$  and mitigating the current crowding around edge defects. The extent of current crowding by edge defects is sample-dependent and is a-priori unknown but tuning  $J(x)$  in-situ by control currents can reduce  $J(\pm w/2)$  to any desirable level at which the resistance of a strip is no longer controlled by penetration of vortices from the edges but is determined by unbinding of vortex-antivortex pairs in the strip, as shown below.

### III. BILAYERS

This chapter addresses tuning  $J(x)$  in bilayers in which two inductively-coupled strips carry antiparallel currents. Two cases are considered: 1. the top and the bottom films in the bilayer are identical and electrically connected at one end, 2. the top and the bottom films made of different superconductors are disconnected and carry different currents.

#### A. Connected bilayers

Consider a bilayer in which two stacked identical films of width  $w$  and thickness  $d$  are separated by a dielectric interlayer of thickness  $h$  and are electrically connected at one end, as shown in Fig. 5. The films carry equal antiparallel currents  $I$  injected into one of the films. The dielectric interlayer is assumed to be thick enough to fully suppress the Josephson coupling of the films and the resulting phase textures<sup>43</sup>.

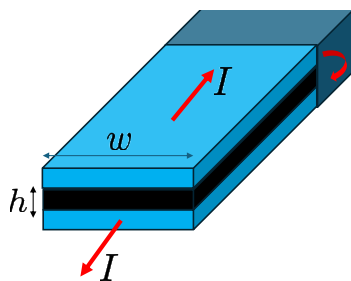


FIG. 5. Two long thin film strips electrically connected at one end and carrying equal antiparallel currents  $I$ . A dielectric interlayer of thickness  $h$  is shown in black.

In this geometry  $Q(x)$  in the top film and  $Q_1(x)$  in

the bottom films are related by  $Q(x) = -Q_1(x)$ , so the solution of Eq. (1) takes the form:

$$A(x, y) = \frac{dw}{8\pi\lambda^2} \int_{-1}^1 \ln[(x-u)^2 + y^2] Q(u) du - \frac{dw}{8\pi\lambda^2} \int_{-1}^1 \ln[(x-u)^2 + (y+h)^2] Q(u) du$$

Setting here  $A(x, 0) = Q(x) - \phi_0\theta'_0/2\pi$  at  $y = 0$  yields the self-consistency equation for  $Q(x)$ :

$$Q(x) - k \int_0^1 \ln \left[ \frac{(x^2 - u^2)^2}{(x^2 + h^2 - u^2)^2 + 4h^2u^2} \right] Q(u) du = \alpha, \quad (8)$$

where  $k = w/4\pi\Lambda$  and  $\alpha = \phi_0\theta'_0/2\pi$ . The sheet current densities  $J = 2Q(x)/\mu_0\Lambda$  calculated from Eq. (8) for different layer spacings  $h$  are shown in Fig. 6. Here  $J(x)$

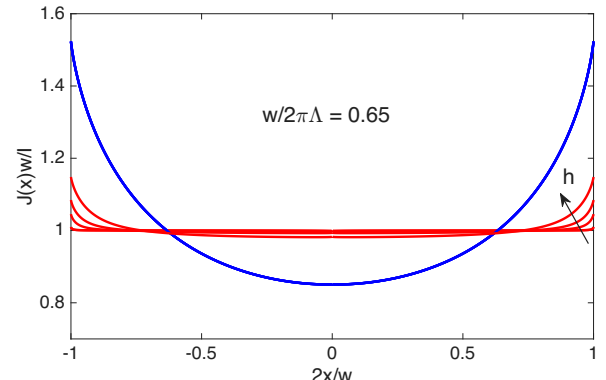


FIG. 6.  $J(x)$  in the bilayer shown in Fig. 4. Calculations were done for  $w/2\pi\Lambda = 0.65$  ( $w = 1$  mm for  $W_{0.8}Si_{0.2}$ ) and different interlayer spacings:  $h/w = 0.005, 0.025, 0.05, 0.1$ . For these  $h$ , the current density at the edge normalized to  $\bar{J} = I/w$  reaches 1.0095, 1.045, 1.084, 1.15, respectively

is nearly flat because two strips with equal antiparallel currents produce no magnetic field far away from the bilayer. Small peaks in  $J(x)$  at the edges result from the field leakage from the interlayer space, the peaks decrease as  $h$  is decreased. The Pearl current crowding practically disappears in a bifilar strip, as it also happens in a strip on a superconducting substrate<sup>41,44,45</sup>.

#### B. Periodic arrays

Consider a periodic structure of bilayers shown in Fig. 7 which can be relevant to SNSPD arrays. Here films in each bilayer are connected as shown in Fig. 5, but the neighboring bilayers are electrically disconnected and carry the same current  $I$  injected by independent current supplies. In this case the solution for  $Q(x)$  is given by

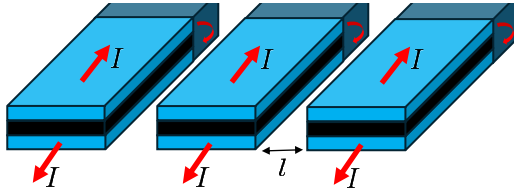


FIG. 7. Periodic array of bilayers spaced by  $l$ .

Eq. (7) summed up over all bilayers:

$$Q(x) - k \sum_n \int_0^1 du Q(u) \times \ln \left[ \frac{[(x - u_n)^2 - u^2]^2}{[h^2 + (x - u_n - u)^2][h^2 + (x - u_n + u)^2]} \right] = \alpha, \quad (9)$$

where  $u_n = n(2 + l)$ ,  $n = 0, \pm 1, \pm 2, \dots$

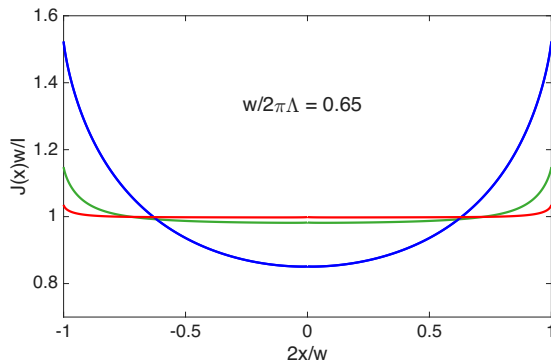


FIG. 8. Comparison of  $J(x)$  for a single film (blue), single bilayer (green) and periodic array (red) calculated for  $w/2\pi\Lambda = 0.65$ ,  $h = 0.1w$  and  $l = 0.01w$ .

Shown in Fig. 8 is  $J(x)$  in the periodic array in comparison with a single bilayer and a bare strip. One can see that peaks in  $J(x)$  at the edges in a periodic array are further reduced as compared to a single bilayer due to partial cancellation of magnetic fields leaking out from the neighboring bilayers. Thus, the Pearl current crowding in a periodic array of connected bilayers can be practically eliminated, no matter how wide the bilayers are. Yet this structure does not provide controllable dips in  $J(x)$  mitigating the edge defects, as it happens in a strip between side control wires.

### C. Bilayers tuned by current

Consider now a bilayer structure which provides no Pearl current crowding and controllable dips in  $J(x)$  at the edges. This can be achieved with two disconnected strips made of different superconductors and carrying different currents  $I$  and  $I_1$  injected to each film separately as shown in Fig. 9. Here the magnetic field produced by

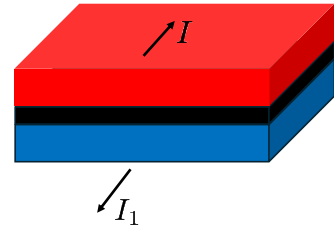


FIG. 9. A bilayer comprised of different superconducting films in which the magnetic field produced by the bottom layer is used to tune  $J(x)$  in the top layer.

the bottom film is used to tune  $J(x)$  in the top (detector) film, similar to the side control wires discussed above.

The equations for  $Q(x)$  and  $Q_1(x)$  in the top and the bottom films, respectively are obtained in the same way as before for a detector film with current control wires:

$$Q(x) - 2k \int_0^1 \ln|x^2 - u^2| Q(u) du - k_1 \int_0^1 \ln[(u^2 + h^2 - x^2)^2 + 4h^2 x^2] Q_1(u) du = \alpha \quad (10)$$

$$Q_1(x) - 2k_1 \int_0^1 \ln|x^2 - u^2| Q_1(u) du - k \int_0^1 \ln[(u^2 + h^2 - x^2)^2 + 4h^2 x^2] Q(u) du = \beta \quad (11)$$

These equations were solved as described in Appendix A. The results presented in Fig. 10 show that the control underlayer with  $\Lambda_1 \ll \Lambda$  effectively flattens  $J(x)$  in most part of the top layer, while reducing  $J(x)$  at the edges. The overall tuning effect of side wires and underlayer on  $J(x)$  in the strip appear very similar, yet the bilayer geometry might be advantageous for SNSPD arrays as it provides higher packing density with fewer control wires.

## IV. NONLINEAR CURRENT PAIRBREAKING

The above results were obtained by solving the London equation (1) in which  $\mathbf{J} = -2\mathbf{Q}/\mu_0\Lambda$  depends linearly on the superfluid velocity at  $Q(x) \ll Q_{c0} = \phi_0/2\pi\xi$ . As the current  $I$  is increased,  $J(Q)$  becomes a nonlinear function of  $Q$  with  $\partial J/\partial Q = 0$  at the depairing current density  $J = J_d$ . This nonlinearity becomes most essential at the edges of wide strips due to the Pearl current crowding.

### A. GL current crowding in a strip

In this section manifestations of the nonlinearity of  $J(Q)$  are evaluated for the GL current density:

$$\mathbf{J} = -2\mathbf{Q}[1 - (Q/Q_{c0})^2]/\mu_0\Lambda. \quad (12)$$

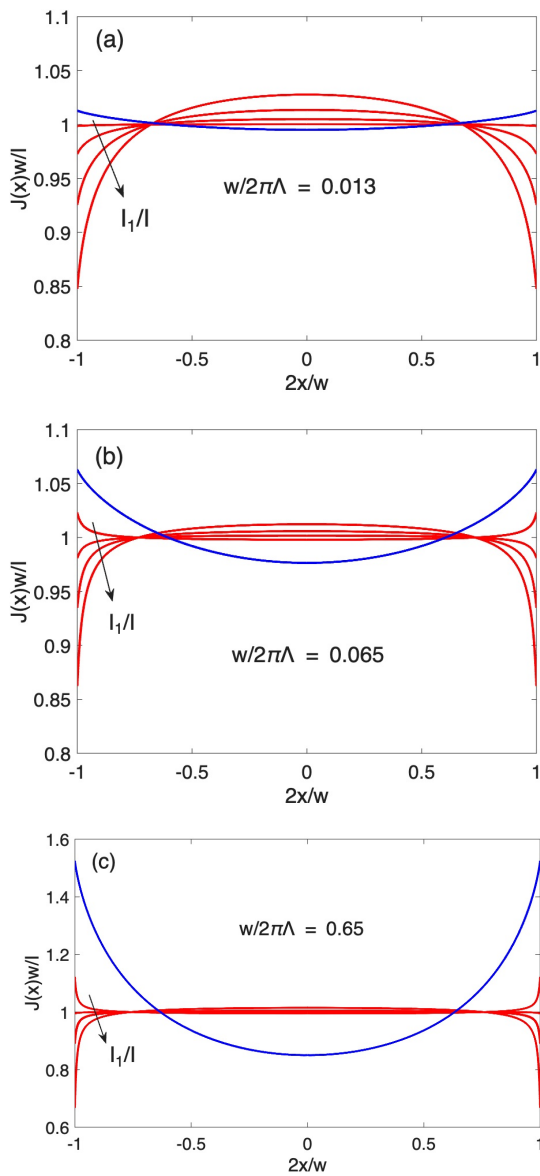


FIG. 10. Sheet current density  $J(x)$  in a top layer of a bilayer calculated for different film widths  $w$  and normalized currents  $I_1/I$  in the bottom layer for  $W_{0.8}Si_{0.2}$  films with  $d = 4$  nm,  $\Lambda = 245$   $\mu\text{m}$ <sup>42</sup>,  $k_1 = 200k$  and  $h = 0.0025w$ : (a)  $w \approx 20 \mu\text{m}$ ,  $I_1/I = -1.2, -4.61, -10.81, -21.06$ , (b)  $w \approx 100 \mu\text{m}$ ,  $I_1/I = 0, -1.88, -3.94, -7.17$ , (c)  $w \approx 1 \text{ mm}$ ,  $I_1/I = 0, -1.09, -1.93, -3.92$ .

Consider first  $J(x)$  in a strip with no control wires. In this case the integral equation for a dimensionless gauge-invariant vector potential  $q(x) = Q(x)/Q_{c0}$  is obtained in the same way as Eq. (5):

$$q(x) - 2k \int_0^1 \ln |x^2 - u^2| q(u) [1 - q^2(u)] du = \gamma, \quad (13)$$

where  $\gamma = \theta'\xi$  and the GL nonlinearity affects the self-field nonlocal term. For a narrow strip with  $k \ll 1$ ,

Eq. (13) yields constant  $q \rightarrow \gamma$  and  $J \rightarrow \phi_0 \theta' [1 - (\xi \theta')^2]/\pi \mu_0 \Lambda$ , the depairing limit is reached at  $\gamma = 1/\sqrt{3}$ . For wider strips, Eq. (13) was solved iteratively:

$$q_{n+1}(x) = 2k \int_0^1 \ln |x^2 - u^2| [q_n(u) - q_n^3(u)] du + \gamma, \quad (14)$$

which gives rapidly converging solutions at  $w \leq 5\Lambda$ . Shown in Fig. 11 are  $Q(x)$  calculated from Eqs. (14) at currents for which  $Q(\pm w/2)$  at the edges reaches the GL depairing limit  $Q_c = Q_{c0}/\sqrt{3} = \phi_0/2\sqrt{3}\pi\xi$ . Here  $Q(x)$  is maximum at the edges and the inhomogeneity of  $Q(x)$  increases with the strip width, similar to that calculated above in the linear London model.

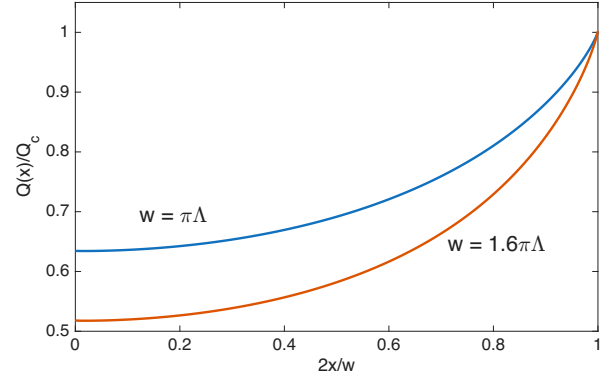


FIG. 11.  $Q(x)$  calculated by solving Eq. (14) at currents for which  $Q(x)$  at the edge reaches the GL depairing limit  $Q_c = Q_{c0}/\sqrt{3}$  for the strip widths  $w = \pi\Lambda$  and  $w = 1.6\pi\Lambda$ .

Unlike  $Q(x)$ , the GL current density  $J(x)$  calculated from Eqs. (12) and (14) can exhibit weaker current crowding than  $J(x)$  of the London model, as shown in Fig. 12. Because the London model describes  $J(x)$  at small currents, the shape of  $J(x)$  changes from the red one at  $I \ll I_d$  to the blue one at  $I \sim I_d$  in Fig. 12. Thus, the Pearl current crowding weakens as  $I$  increases and becomes minimum if  $J(\pm w/2)$  at the edges reaches  $J_d$ .

Shown in Fig. 13 is the current crowding ratio  $J(w/2)/J(0)$  as a function of the normalized strip width  $w/2\pi\Lambda$  calculated from the London theory at  $I \ll I_d$  and the GL theory at  $I \sim I_d$ . As  $I$  is increased, the ratio  $J(w/2)/J(0)$  for a given  $w$  decreases from its maximum on the red curve at  $I \ll I_d$  to its minimum on the blue curve at  $I \approx I_d$ , so the London model overestimates the Pearl current crowding in wide strips at  $I \sim I_d$ .

## B. Strip with current control wires

Consider the effect of GL nonlinearity on  $J(x)$  in a strip between two control wires carrying equal currents. The equation for  $q(x)$  is obtained in the same way as it

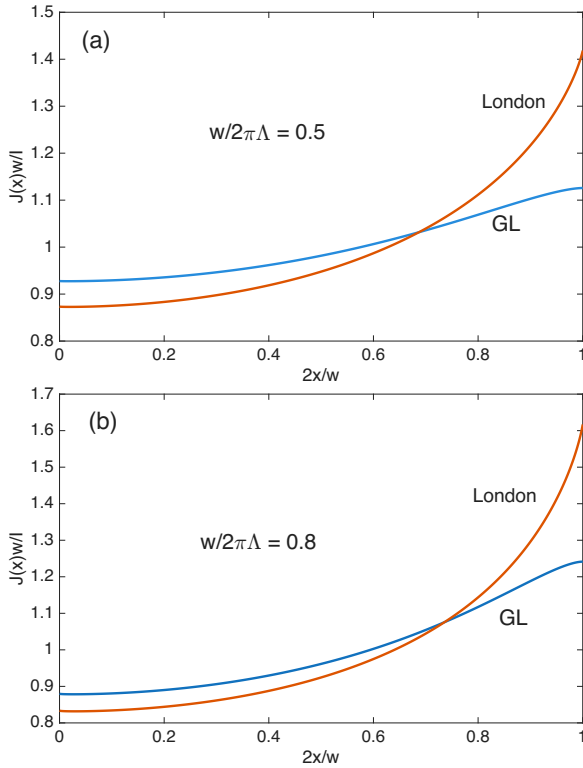


FIG. 12. Sheet current densities  $J(x)$  calculated from the London and the GL theories at the same driving parameter  $\gamma$  at which the GL current density reaches  $J_d$  at the edges for different strip widths: (a)  $w = \pi\Lambda$ , (b)  $w = 1.6\pi\Lambda$ .

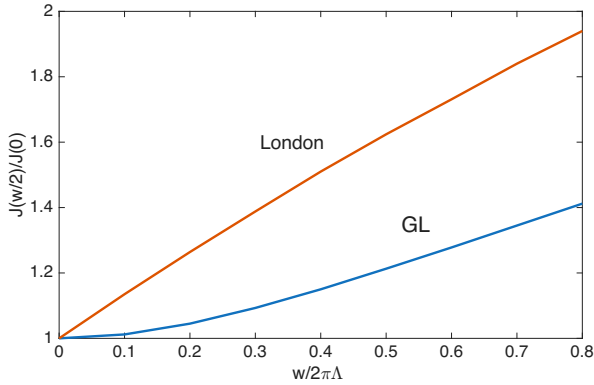


FIG. 13. The current crowding ratio  $J(w/2)/J(0)$  calculated in the London limit of  $I \ll I_d$  and the GL pairbreaking limit for which  $J(x)$  at the edge reaches  $J_d$ .

was done in Sec. II.

$$q(x) - 2k \int_0^1 \ln |x^2 - u^2| [q(u)1 - q^3(u)] du - \quad (15)$$

$$k_1 \int_{1+b}^{1+l+b} \ln[(u^2 + h^2 - x^2)^2 + 4h^2 x^2] p(u) du = \gamma_0,$$

$$p(x) - 2k_1 \int_{1+b}^{1+b+l} \ln |x^2 - u^2| p(u) du - \quad (16)$$

$$k \int_0^1 \ln[(u^2 + h^2 - x^2)^2 + 4h^2 x^2] [q(u) - q^3(u)] du = \gamma_1,$$

where  $q = Q_0(u)/Q_{c0}$ ,  $p = Q_1(u)/Q_{c0}$ , the dimensionless phase gradients  $\gamma_0 = \xi\theta'_0$  and  $\gamma_1 = \xi\theta'_1$  are expressed in terms of currents  $I$  and  $I_1$  as described in Appendix A and  $\xi$  is the coherence length in the strip. Here the control wires of the same dimensions and material and carrying equal currents are considered.

Equations (15) and (16) were solved iteratively, as described in the previous subsection, assuming the linear London relation  $J = -2Q_1/\mu_0\Lambda_1$  in the control wires. Shown in Fig. 14 are representative examples of  $J(x)$  calculated from Eqs. (15) and (16) for the current  $I$  at which  $J(x)$  in the center of the strip reaches  $J_d$ . The

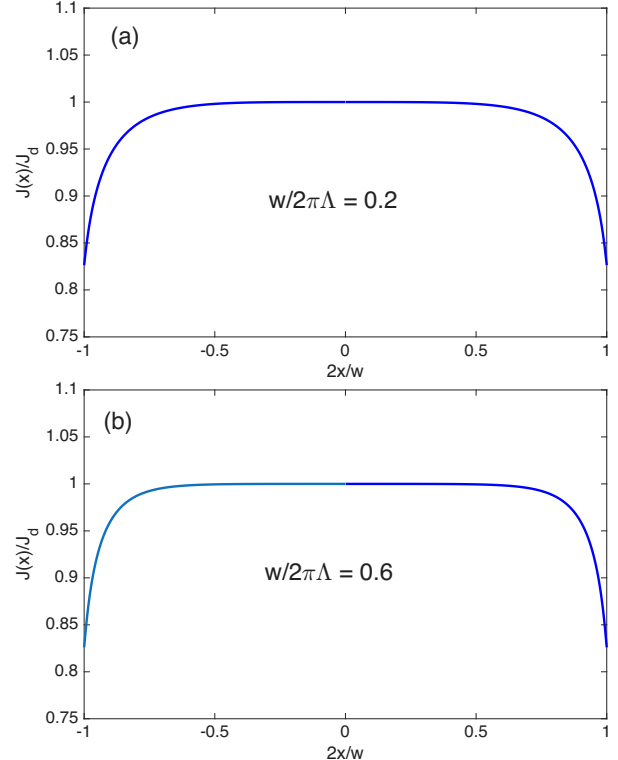


FIG. 14.  $J(x)$  calculated from Eqs. (15)-(16) at a current  $I$  at which the maximum  $J(x)$  reaches  $J_d$  in the central part of the strip. The calculations were done at  $k_1 = 500k$ ,  $l = 0.15w$ ,  $b = h = 5 \cdot 10^{-3}w$  and: (a)  $w = 1.26\Lambda$ ,  $I = 0.983I_d$ ,  $I_1 = 1.34I$ ; (b)  $w = 3.77\Lambda$ ,  $I = 0.988I_d$ ,  $I_1 = 0.78I$ .

behavior of  $J(x)$  at  $I \simeq I_d$  is qualitatively similar to that

of the London model at  $I \ll I_d$  shown in Fig. 4. Yet the GL nonlinearity reduces a small hump in  $J(x)$  in the middle of the strip obtained in the London model and makes  $J(x)$  nearly flat except for tunable dips in  $J(x)$  at the edges. The GL flattening of  $J(x)$  results in a more uniform sensitivity of SNSPD to photons. Depending on the magnitude of  $I_1$ , the maximum in  $J(x)$  can occur either in the middle of the strip or closer to the edge as  $I_1$  is decreased. Such non-monotonic  $J(x)$  resulting from interplay of the Pearl current crowding and the dips in  $J(x)$  at the edges is also visible in Fig. 4c.

The above results were obtained assuming that the current density in the side wires does not exceed the pair-breaking limit. This is indeed the case of control wires made of a superconductor with  $\Lambda_1 \ll \Lambda$ . For instance, for a 4 nm thick  $W_{0.8}Si_{0.2}$  film with  $\lambda = 700$  nm<sup>42</sup>, we have  $\Lambda = 245 \mu\text{m}$ . For the side wires made of a moderately clean Nb with  $\lambda_1 \simeq 50$  nm and  $\xi_1 \simeq 32$  nm, the ratio  $\Lambda_1/\Lambda = 500$  used in the calculations implies a 10 nm thick side strip. Shown in Fig. 15 is a normalized superfluid velocity  $Q_1(x)/Q_{c0}$  in the control wires calculated for the same input parameters as in Fig. 14(b). Here the asymmetric  $Q_1(x)$  in the side strip of width  $l = 0.15w \simeq 95\Lambda_1$  results from its inductive coupling with the central strip and another control wire. Yet even the highest peak in  $Q_1(x) \simeq 0.045Q_{c0} \simeq 0.36Q_{c1}$  is well below the GL depairing limit  $Q_{c1} = \phi_0/2\sqrt{3}\pi\xi_1$  so the London electrodynamics in the side strip is applicable.

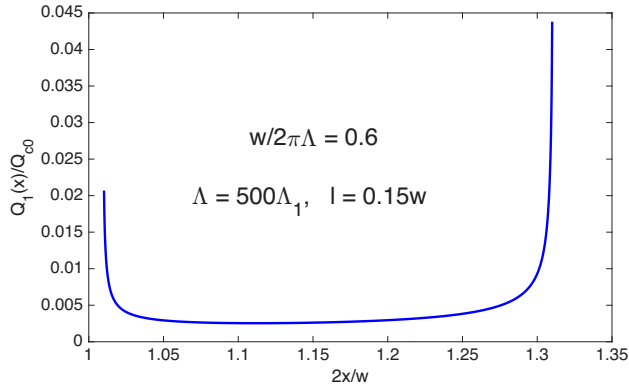


FIG. 15.  $Q_1(x)/Q_{c0}$  in the control strip calculated from Eqs. (15)-(16) at  $k_1 = 500k$ ,  $l = 0.15w$ ,  $b = h = 5 \cdot 10^{-3}w$ ,  $w = 3.77\Lambda$ ,  $I = 0.988I_d$ ,  $I_1 = 0.78I$ .

### C. Superconducting diode

Current flow in a strip coupled inductively with control wires depends on the relative orientation of  $I$  and  $I_1$ . The control wires cause dips in  $J(x)$  at the strip edges if currents in the strip and the wires flow in the same direction. For antiparallel  $I$  and  $I_1$ , the self field of the wires increases  $B_z(x)$  at the edges, enhancing the current crowding in the strip. In a bilayer shown in Fig. 9,

the Pearl current crowding is reduced if  $I$  and  $I_1$  are antiparallel and enhanced if both  $I$  and  $I_1$  flow in the same direction. Because of such current non-reciprocity, the structures considered above behave as superconducting diodes in which the critical currents of switching to a resistive state depend on the polarity of  $I$  at a fixed  $I_1$ . The idea that the control wires can cause polarity-dependent critical current was first implemented by Brenneman in the in-line cryotron with a 900 nm thick and 9 mm wide Sn film<sup>39</sup> and by Swartz and Hart on  $1 \mu\text{m} \times 1 \text{ mm} \times 1 \text{ cm}$   $Pb_{0.9}Tl_{0.1}$  ribbon coupled with Cu control wires<sup>40</sup>. Recently TDGL simulations of the vortex diode were done for the geometry shown in Fig. 2<sup>46</sup>. However,  $\mathbf{J}(x, y)$  in Ref. 46 was not calculated self-consistently by matching  $\mathbf{Q}(x, y)$  with the solution of the Maxwell equations for  $\mathbf{H}(x, y)$  outside the strip but evaluated using an ad-hoc boundary condition  $H_y(w/2) = \mu_0 w j(w/2)$  inconsistent with  $H_y(w/2) \simeq \mu_0 j d \ln(w/d)$  for a thin strip. Here the diode effect is calculated for a thin strip in the Pearl limit with  $d \ll \lambda$  and  $\Lambda \gg \lambda$  characteristic of SNSPDs with  $\kappa \sim 10^2$  and  $d < \xi$ <sup>3-5</sup>, using the self-consistent approach developed in this work.

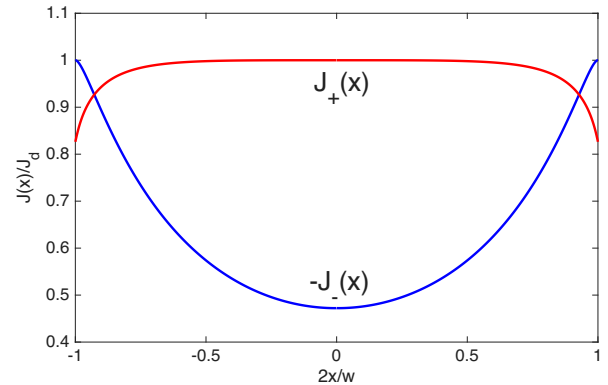


FIG. 16. Current distributions in a strip calculated from Eqs. (15) and (16) for parallel  $J_+(x)$  and antiparallel  $J_-(x)$  current flow with respect to a fixed control current  $I_1$ . The critical currents are  $I_c^+ = 0.983I_d$  and  $I_c^- = -0.63I_d$  at  $I_1 = 1.32I_d$ ,  $w = 1.26\Lambda$ ,  $k_1 = 500k$ ,  $l = 0.15w$ ,  $b = h = 5 \cdot 10^{-3}w$ , where  $J_d$  is the depairing current density in the strip.

Shown in Fig. 16 are the sheet current densities  $J_+(x)$  and  $J_-(x)$  in a strip calculated from Eqs. (15) and (16) for parallel and antiparallel  $I$  and  $I_1$ , respectively. Here the control current  $I_1$  was fixed, and  $J_+(x)$  and  $J_-(x)$  were calculated at critical currents  $I_c^+$  and  $I_c^-$  at which  $J(x)$  reached  $J_d$  either in the center or the edges of the strip. For parallel  $I$  and  $I_1$ , the depairing limit is first reached in the center, while for antiparallel  $I$  and  $I_1$ , it happens at the edges. As a result, the critical currents  $I_c^+$  and  $I_c^-$  given by the areas under the curves in Fig. 16 become markedly different, the difference between  $I_c^+$  and  $I_c^-$  increases as the control current  $I_1$  is increased.

The critical currents  $I_c^+$  and  $I_c^-$  were calculated for different  $I_1$  ranging from 0 to  $2.2I_d$  and other parameters specified in the caption of Fig. 16. Using the

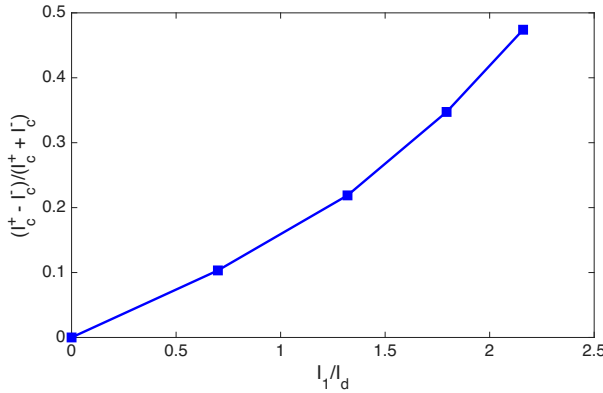


FIG. 17. The diode efficiency parameter as a function of the normalized control current calculated at  $w = 1.26\Lambda$ ,  $k_1 = 500k$ ,  $l = 0.15w$ ,  $b = h = 5 \cdot 10^{-3}w$ .

so-obtained  $I_c^+(I_1)$  and  $I_c^-(I_1)$ , the diode parameter  $(I_c^+ - I_c^-)/(I_c^+ + I_c^-)$  was calculated as a function of  $I_1$ . The result shown in Fig. 17 suggests that such vortex diode can be quite efficient as it is controlled by current *in situ* and does not require any external magnetic field. This distinguishes this superconducting diode from other propositions in which the non-reciprocal current response requires an external magnetic field combined with spatial inhomogeneity of materials properties, edge indentations, superconducting-ferromagnetic structures, spin-orbital effects, or unconventional superconductivity with nonzero momentum of Cooper pairs (see, e.g., reviews<sup>47–49</sup> and the references therein).

## V. VORTEX RESISTIVE STATES TUNABLE BY CONTROL WIRES

Engineering supercurrent flow in a strip by control wires allows tuning resistive states caused by the motion of vortices. As  $I$  exceeds either  $I_c^+$  or  $I_c^-$ , the strip switches to a flux flow state, the mechanisms of resistivity depending on the polarity of current. For parallel  $I$  and  $I_1$ , there are two possibilities: 1.  $I_1$  is not strong enough to deactivate the Pearl current crowding and the edge defects. In this case the resistance is caused by penetration of vortices and antivortices from the opposite edges of the strip. 2. If  $I_1$  is sufficient to fully deactivate the current crowding and the edge defects, the resistive transition at  $I = I_c^+$  occurs due to unbinding of vortex-antivortex (VAV) pairs<sup>36,37</sup> in the strip, where  $J(x)$  can be close to  $J_d$ . For antiparallel  $I$  and  $I_1$ , the enhanced current crowding at the edges ensures that  $J(x)$  first reaches  $J_d$  at the edges. In this case the resistance is caused by penetration of vortices and antivortices and their annihilation in the center at  $I > I_c^-$ , as depicted in Fig. 18

This section primarily focuses not on a self-field flux flow resistance at  $I > I_c^\pm$  but on a small voltage  $V(I, T)$  at subcritical currents. The behavior of  $V(I, T)$  at  $I < I_c^\pm$  determines the dark count rate in photon de-

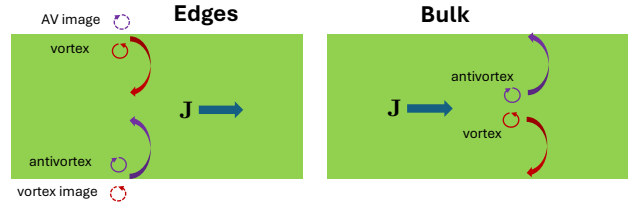


FIG. 18. Single vortices and antivortices penetrating from the film edges and VAV pair unbinding inside the strip.

tectors and also can be a sensitive indicator of the transition from the edge-dominated to the bulk-dominated resistance. This transition occurs above the threshold control current  $I_1 > I_1^*$  which depends on the strip width and the degree of current crowding caused by edge defects. Here thermally-activated uncorrelated hopping of sparse vortices and non-overlapping VAV pairs is considered, leaving aside effects of vortex interaction<sup>37</sup> and quantum tunneling of vortices at ultra low  $T$ <sup>50,51</sup>.

The rate  $S_e$  of thermally-activated hopping of vortices through the edge is determined by the energy of the vortex  $E_v(u)$  which can be written as a work to move a vortex by a distance  $u$  from the edge of the strip:

$$E(u) = E_v(u) - \phi_0 \int_0^u J(x) dx, \quad (17)$$

where  $E(u) = 0$  at the strip edges<sup>52,53,56</sup>. The last term in Eq. (17) is the work of the Lorentz force of transport current density  $J(x)$  calculated above for different geometries. The self-energy  $E_v(u)$  is the work against the attraction force between the vortex and the edges of the strip. Derivation of  $E_v(u)$  in a strip of arbitrary width<sup>52</sup> given in Appendix B results in:

$$E_v(u) = \epsilon \ln \left[ \frac{w}{\pi \xi} \sin \left( \frac{\pi u}{w} \right) \right] + 2\epsilon \sum_{n=1}^{\infty} \sin^2 \left( \frac{\pi u n}{w} \right) \times \left[ \frac{4}{\pi \sqrt{n^2 - (w/\pi \Lambda)^2}} \tan^{-1} \left[ \frac{n - w/\pi \Lambda}{n + w/\pi \Lambda} \right] - \frac{1}{n} \right]. \quad (18)$$

Here  $\epsilon = \phi_0^2/2\pi\mu_0\Lambda$  is the vortex line energy,  $\xi = 0.34\xi$  and the factor 0.34 accounts for the vortex core energy obtained from the GL calculations<sup>53,56</sup>. For a narrow strip with  $w \ll \pi\Lambda$ , Eqs. (17) and (18) yield<sup>52,56</sup>:

$$E_v(u) = \epsilon \ln \left( \frac{w}{\pi \xi} \sin \frac{\pi u}{w} \right) - \phi_0 J u, \quad (19)$$

This result (without the core energy) first obtained in Ref. 54 for a vortex in a narrow superconducting strip also follows from a complex velocity potential of a vortex in an ideal liquid in a channel<sup>55</sup>.

The vortex energy  $E_v(u)$  for different widths  $w$  calculated from Eq. (18) is shown in Fig. 19. As  $w$  is increased,  $E_v(u)$  flattens in the central part of the strip

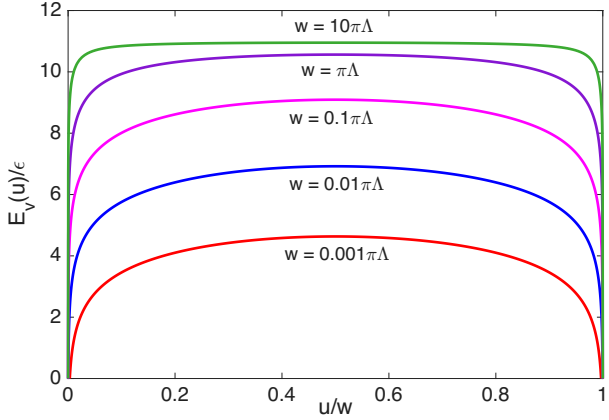


FIG. 19. The self energy of a vortex  $E_v(u)$  calculated from Eq. (18) for different strip widths with the parameters  $\Lambda = 245 \mu\text{m}$ ,  $\xi = 7 \text{ nm}$  of a 4 nm thick  $\text{W}_{0.8}\text{Si}_{0.2}$  film<sup>42</sup>. Narrow regions of  $u \lesssim \xi$  at the edges, where the London theory is not applicable are excluded.

and approaches  $E_v \simeq \epsilon \ln(\Lambda/\xi)$  at  $w \gg \Lambda$  (see also Ref. 57). The energy barrier of vortex hopping across the strip  $U \simeq \epsilon \ln(w/\xi)$  at  $J = 0$  increases slowly with the width at  $w < \Lambda$  and levels off at  $\simeq \epsilon \ln(\Lambda/\xi)$  if  $w \gg \Lambda$ . Transport current shifts the maximum in  $E(u)$  from the middle of the strip to the position  $u_m(J)$  closer to the edge, where  $u_m$  readily follows from Eq. (19):

$$u_m = \frac{w}{\pi} \cot^{-1} \frac{J}{J_0}, \quad (20)$$

$$J_0 = \frac{\pi \epsilon}{\phi_0 w} = \frac{\phi_0}{2\mu_0 w \Lambda} \sim \frac{\xi}{w} J_d \ll J_d \quad (21)$$

The London model becomes invalid for a vortex spaced by  $u \sim \xi$  from the edges. Numerical GL calculations of  $E_v(u)$ <sup>56</sup> have shown that the London model captures the behavior of  $E_v(u_m)$  if  $J$  is not too close to  $J_d$ , and that the energy barrier at  $J = J_d$  vanishes. To take this effect into account, we define the energy barrier for the vortex entry as  $U_e = E[u_m(J)] - E[u_m(J_d)]$ , where  $E(u)$  and  $u_m$  are given by Eq. (19) and (20). At  $J \gg J_0$  this yields  $U_e$  independent of the film width:

$$U_e = \epsilon \ln(J_d/J), \quad J \gg J_d \xi / w. \quad (22)$$

This gives a reasonable approximation of  $U_e(J)$  at  $J \simeq J_d$  at which  $u_m \sim \xi \ll w$  is close to the edge of the film, as depicted in Fig. 20. Thermally-activated hopping of vortices over the edge barrier results in a mean dc voltage  $V = V_0(J/J_d)^{\epsilon/T}$ , where  $V_0$  was evaluated in<sup>52</sup>. At  $\epsilon/T \gg 1$  and  $J \simeq J_d$  the V-I curve takes the form:

$$V = V_0 \exp[-U/T], \quad U \simeq \epsilon(1 - J/J_d). \quad (23)$$

The probability of thermally-activated penetration of a vortex from an ideal film edge is proportional to the Arrhenius factor  $\propto \exp(-U_e/T)$  which can increase substantially due to edge defects which locally reduce  $U(z, J)$

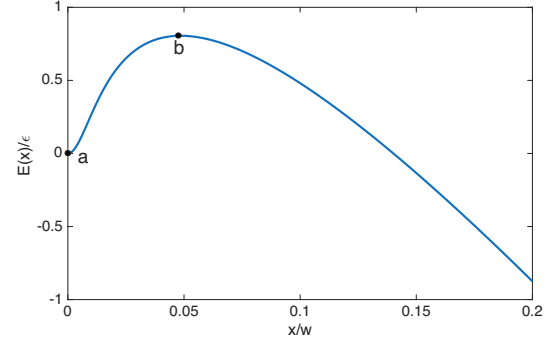


FIG. 20. Qualitative dependence of  $E(x)$  on the vortex position evaluated from Eqs. (19) regularized by  $x \rightarrow \tilde{x} = [x^2 + \xi^2]^{1/2}$ ,  $E(x) \rightarrow E(\tilde{x}) + \phi_0 J \tilde{\xi}$ ,  $\tilde{\xi} = 10^{-2} w$  and  $J = 20 J_0$ .

and facilitate penetration of vortices, as shown in Fig. 1. Here the averaged Arrhenius factor  $\langle \exp[-U_e(J, z)/T] \rangle$  is dominated by strong defects like sharp indentations causing significant local current crowding. Given many uncertainties depending on the film growth and deposition parameters and also on whether the edge cross-section is rectangular or rounded<sup>58,59</sup>, it is assumed here that edge defects locally increase an averaged current density in a narrow belt along the edge depicted by a dashed line in Fig. 1. In this case  $U_e(I) = \epsilon(1 - \zeta_1 J_e/J_d)$ , where the current density at the strip edges  $J_e(I, I_1)$  was calculated above for different geometries, and the current crowding factor  $\zeta_1 > 1$  accounts for the defect-mediated enhancement of  $J(x)$  at the edges.

The number  $S_e$  of thermally-activated vortices penetrating over the edge barrier per unit time in a strip of length  $L$  can be evaluated as follows:

$$S_e = S_{e0} \exp \left[ -\frac{\epsilon}{T} \left( 1 - \frac{\zeta_1 J_e}{J_d} \right) \right], \quad S_{e0} \sim \frac{L \nu}{l_i} \quad (24)$$

Here  $L/l_i$  is a number of statistically-independent vortex entries through the edge defects with a mean spacing  $l_i$  and  $\nu$  is an attempt frequency. Equal contributions of vortices and antivortices penetrating from the opposite edges of the strip are included in the definition of  $l_i$ . For overdamped Abrikosov vortices,  $\nu \simeq \sqrt{k_a k_b}/4\pi\eta$  follows from the classical result of Kramers<sup>60</sup>, where  $k_a$  and  $k_b$  are curvatures of  $E(x)$  at the bottom and the top of the potential well depicted in Fig. 20,  $\eta = \phi_0^2 d / 2\pi \xi^2 \rho_n$  is the Mattis-Bardeen vortex drag coefficient, and  $\rho_n$  is the normal state resistivity. Taking  $\sqrt{k_a k_b} \sim \phi_0^2 d / 4\pi \mu_0 \lambda^2 \xi^2$  at  $J \sim \tilde{J}_d$  in Eq. (24) yields

$$S_{e0} \sim \frac{L R_{\square}}{4\pi \mu_0 \Lambda l_i} \quad (25)$$

For a 4 nm thick  $\text{W}_{0.8}\text{Si}_{0.2}$  film with  $L = 1 \text{ mm}$ ,  $\Lambda = 245 \mu\text{m}$ ,  $R_{\square} = \rho_n/d = 340 \Omega$ <sup>42</sup> and  $l_i \sim 10^2 \text{ nm}$ , we get  $\epsilon \approx 150 \text{ K}$  and  $S_{e0} \sim 10^{14} \text{ s}^{-1}$ . Here Eq. (25) is no more than a rough estimate which takes into account neither microstructural details of edge imperfections nor

deformation of the vortex core at the edge in the presence of current <sup>56</sup> nor local variations of  $U_e(z, I)$  along the edges which may add a power-law factor  $(1 - J_e/J_d)^n$  with  $n \sim 1$ . Yet the logarithmic slope

$$\frac{d \ln S_e}{dI} = \frac{\epsilon \zeta_1}{TI_d} \quad (26)$$

is practically insensitive to the uncertainties in  $S_{e0}$  and its possible power-law dependence on  $I$  if  $T \ll \epsilon$ . From Eq. (24), one can get a maximum current  $I_{c1}$  which can flow in SNSPD at an operational dark count rate  $S_c$ :

$$I_{c1} = \frac{I_d}{\zeta_1 \zeta_2} \left( 1 - \frac{T}{\epsilon} \ln \frac{S_{e0}}{S_c} \right), \quad (27)$$

where  $\zeta_2$  relates  $J_e = \zeta_2 \bar{J}$  with the mean current density  $\bar{J} = I/w$ . The factor  $\zeta_2$  can be larger than 1 in a bare strip or smaller than 1 in a strip with control wires producing an inverted  $J(x)$  profile. For  $S_c = 10^2 \text{ s}^{-1}$ ,  $S_{e0} = 10^{14} \text{ s}^{-1}$  and  $T/\epsilon = 1/150$  at 1 K, Eq. (27) yields  $I_{c1} \approx 0.82 I_d / \zeta_1 \zeta_2$ . Here  $I_{c1}$  decreases logarithmically with  $L$ . The account of a factor  $(1 - I/\tilde{I}_d)^n$  in  $S_{e0}$  only increases  $I_{c1}$  by few % and is neglected hereafter.

Another contribution to  $S$  comes from thermally-activated unbinding of VAV pairs of radius  $r_p \simeq 2\xi J_d / J(x) \ll w$  in the strip <sup>36</sup>. The edge and the bulk contributions to  $S$  are illustrated in Fig. 18, from which it follows that the energy scale of the VAV pair unbinding inside a strip with  $w \gg \xi$  at  $J \sim J_d$  is twice that of the vortices penetrating from the edges:

$$U_b(x) = 2\epsilon \left[ 1 - \frac{J(x)}{J_d} \right], \quad J(x) \sim J_d \quad (28)$$

where  $U_b(x)$  varies slowly over the VAV pair radius  $r_p \simeq 2\xi J_d / J(x) \ll w$ . Notice than neither Eq. (22) for an ideal edge nor Eq. (28) in a uniform strip are applicable at  $J$  gets close to  $J_d$ , where the description in terms of uncorrelated vortices and non-overlapping VAV pairs breaks down <sup>36,37</sup>. Here the notion of the energy barrier for a single vortex becomes ill-defined as the uniform current-carrying state at  $J = J_d$  is unstable with respect to infinitesimal perturbations of the order parameter along the entire strip. If the critical currents  $I_{c1}$  and  $I_{c2}$  are not too close to  $I_d$ , the linear approximations of  $U_e(J)$  and  $U_b(J)$  at  $J \sim J_d$  seems applicable.

The production rate of uncorrelated VAV pairs in a film at  $I \sim I_d$  is evaluated as follows:

$$S_b = \nu L \int_0^w \exp \left[ -\frac{2\epsilon}{T} \left( 1 - \frac{J(x)}{J_d} \right) \right] \frac{dx}{2\pi\xi^2}. \quad (29)$$

Here  $A/2\pi\xi^2$  is a number of statistically-independent positions of the vortex core of radius  $\sqrt{2}\xi$  in a film of area  $A = Lw$ . The total  $S$  is a sum of  $S_e$  and  $S_b$ :

$$S = \nu L \left[ \frac{1}{l_i} e^{-\frac{\epsilon}{T} \left( 1 - \frac{J_e}{J_d} \right)} + \int_{-w/2}^{w/2} e^{-\frac{2\epsilon}{T} \left( 1 - \frac{J(x)}{J_d} \right)} \frac{dx}{2\pi\xi^2} \right]. \quad (30)$$

This equation expresses the dark count rate  $S(I, I_1)$  in terms of  $J(x)$  and  $J_e = J(\pm w/2)$  calculated above for different geometries. In a narrow strip with no control wires  $J(x)$  is uniform so the edge contribution enhanced by the current crowding parameter  $\zeta_1 > 1$  dominates  $S(I, T)$  at  $T \ll \epsilon$ . The edge contribution is further enhanced in wide strips with  $w > \Lambda$  due to the Pearl current crowding.

The control wires can reduce  $J_e$  to the point at which  $S_e$  becomes smaller than  $S_b$ . The above calculations of  $J(x)$  show that, even though the control wires and the GL pairbreaking flatten  $J(x)$  at  $\bar{J} \simeq J_d$ , the current density still has a weak maximum at the center, where  $J(x) \approx J(0) - x^2 J''/2$ . This maximum might affect  $S$  if  $w^2 \epsilon J'' \gtrsim 4T$  so that the VAV contribution mostly comes from a central part of the strip. If  $w^2 \epsilon J'' \gg TJ_d$  the integrand in Eq. (30) is peaked at  $x = 0$  so the integration limits can be extended to infinity, giving:

$$S = S_{e0} \left[ e^{-\frac{\epsilon}{T} \left( 1 - \frac{J_e}{J_d} \right)} + \frac{l_i}{2\xi^2} \sqrt{\frac{TJ_d}{\pi\epsilon J''}} e^{-\frac{2\epsilon}{T} \left( 1 - \frac{J(0)}{J_d} \right)} \right]. \quad (31)$$

If  $J(x)$  is sufficiently flat in the most part of strip ( $w^2 \epsilon J'' \lesssim 4TJ_d$ ), Eq. (30) becomes:

$$S = S_{e0} \left[ e^{-\frac{\epsilon}{T} \left( 1 - \frac{J_e}{J_d} \right)} + \frac{wl_i}{2\pi\xi^2} e^{-\frac{2\epsilon}{T} \left( 1 - \frac{J(0)}{J_d} \right)} \right]. \quad (32)$$

Consider for the sake of clarity the London model in which both  $J_e = \zeta_2 \bar{J}$  and  $J(0) = \zeta_3 \bar{J}$  are proportional to the mean current density  $\bar{J} = I/w$  and the factors  $\zeta_2 < 1$  and  $\zeta_3 > 1$  depend only on  $w/\Lambda$  and  $I_1$ . In the case described by Eq. (32) the VAV unbinding dominates over the edge contribution  $S_e$  if:

$$\frac{\bar{J}}{J_d} (2\zeta_3 - \zeta_1 \zeta_2) > 1 - \frac{T}{\epsilon} \ln \left( \frac{wl_i}{2\pi\xi^2} \right). \quad (33)$$

Clearly, Eq. (33) is not satisfied at  $\bar{J} \ll J_d$  for which the edge contribution is always dominant. However, Eq. (33) can be satisfied at  $J_v < \bar{J} < J_d$ , where

$$J_v = \frac{J_d}{(2\zeta_3 - \zeta_1 \zeta_2)} \left[ 1 - \frac{T}{\epsilon} \ln \left( \frac{wl_i}{2\pi\xi^2} \right) \right]. \quad (34)$$

For,  $l_i = 10\xi$ ,  $T/\epsilon = 1/150$  and  $w/\xi = 10^4$ , the last term in the brackets of Eq. (34) is relatively small:  $(T/\epsilon) \ln(wl_i/2\pi\xi^2) \simeq 0.06$ . In this case the condition  $J_v < J_d$  takes a simple form  $\zeta_1 \zeta_2 (I_1) \lesssim 1$  implying that the control wires produce deep enough dips in  $J(x)$  at the edges to compensate the current crowding effect of lithographic defects. Here  $J_v$  decreases as  $I_1$  increases and may drop down to  $J_v \simeq J_d/2$  at  $\zeta_1 \zeta_2 (I_1) \ll 1$ , given that  $\zeta_3$  is close to 1 in all our numerical results.

Shown in Fig. 21 is an example of how the logarithmic slope  $d \ln S(I) / dI$  calculated from Eq. (32) changes upon increasing  $I_1$  for the material parameters of 3 nm thick WSi detectors investigated in Ref. 38. Here the S-window is confined between the sensitivity floor (dashed line) and the upper limit close to the SNSPD switching

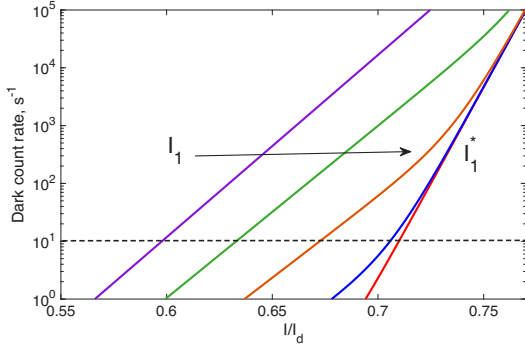


FIG. 21. Change in the logarithmic slope  $d \ln S/dI$  as  $I_1$  is increased calculated from Eq. (33) for  $T = 0.9$  K,  $\epsilon = 66$  K<sup>38</sup>,  $wI_i/\xi^2 = 10^4$ ,  $S_{e0} = 10^{14}$  s<sup>-1</sup>,  $\zeta_1 = 1.1$ ,  $\zeta_3 = 1.05$  and the control current parameters  $\zeta_2 = 0.9, 0.85, 0.8, 0.75, 0.7$ . A jumpwise increase in  $d \ln S/dI$  occurs at  $\zeta_2 \approx 0.7 - 0.75$ , which defines  $I_1^*$  above which  $S$  is dominated by the VAV unbinding.

to the normal state. One can see that decreasing  $\zeta_2$  upon increasing  $I_1$  first causes a nearly parallel shift of  $\ln S$  to higher bios currents followed by an abrupt increase of the slope  $d \ln I/dI$  around a threshold control current  $I_1$  above which the edge vortex contribution is reduced below the sensitivity floor and  $S$  is limited by the VAV pair unbinding. Furthermore, tuning  $I_1$  in the control wires can reduce the dark current rate at a fixed bios current by several orders of magnitude. The behavior of  $S(I, I_1)$  shown in Fig. 21 was observed on WSi SNSPD with Nb control wires<sup>38</sup>. A sharp change of  $d \ln V/dI$  associated with the VAV unbinding upon increasing  $I$  was observed in narrow NbN meandering nanowires<sup>61</sup>.

At  $I_1 > I_1^*$  penetration of vortices from the edges is suppressed and the dark count rate limited by the VAV unbinding. In the simplest case of a flat  $J(x)$  profile in the most part of the strip, Eq. (32) reduces to:

$$S = S_{b0} \exp \left[ -\frac{2\epsilon}{T} \left( 1 - \frac{\zeta_3 I}{I_d} \right) \right], \quad (35)$$

$$S_{b0} \sim \frac{AR_{\square}}{8\pi^2\mu_0\Lambda\xi^2}, \quad I_1 > I_1^*. \quad (36)$$

The critical current  $I_{c2}$  limited by the VAV pair unbinding at a given dark count rate criterion  $S_c$  is then:

$$I_{c2} = \frac{I_d}{\zeta_3} \left( 1 - \frac{T}{2\epsilon} \ln \frac{S_{b0}}{S_c} \right). \quad (37)$$

For  $A = 20 \mu\text{m} \times 1 \text{ mm}$ ,  $R_{\square} = 340 \Omega$ ,  $\Lambda = 245 \mu\text{m}$ ,  $\xi = 7 \text{ nm}$ <sup>42</sup> and  $T/2\epsilon = 1/300$ , Eqs. (35)-(37) give  $S_{b0} \sim 6 \cdot 10^{18} \text{ s}^{-1}$  and  $I_{c2} \approx 0.87 I_d / \zeta_3$  at  $S_c = 10^2 \text{ s}^{-1}$ . Here  $I_{c2}$  decreases logarithmically with the SNSPD area.

Neither the current crowding parameter  $\zeta_1$  of lithographic defects nor the depairing currents  $I_d$  for a particular SNSPD are really known and they can hardly be directly measured. Usually  $I_d$  is evaluated from the measurements of the dependence of kinetic inductance on the bios current calculated from the BCS model for a narrow

strip with  $w \ll \Lambda$  in the dirty limit<sup>62</sup>. However, this model does not account for the realistic electron-phonon pairing of the Eliashberg theory<sup>63</sup>, nonequilibrium<sup>64</sup> or Joule heating<sup>65</sup> effects, a contribution from the Josephson inductance of grain boundaries<sup>66</sup> or the reduction of  $J_d$  by subgap quasiparticle states<sup>67</sup> which are especially pronounced in thin films<sup>68</sup>. Yet tuning  $J(x)$  *in situ* by control wires and detecting the abrupt change in  $d \ln S/dI$  at  $I_1 \approx I_1^*$  ensures reaching the ultimate photon sensitivity at  $I = I_{c2}$  limited only by the VAV unbinding in a particular SNSPD, even if neither  $J_d$  nor the extent of current crowding at the edge defects is known.

## VI. DISCUSSION

This work shows that integration of a thin film superconducting strip with current-carrying control wires can be used to engineer a desired profile of supercurrent density  $J(x)$  with no current crowding at the edges in a strip wider than the Pearl length. Here  $J(x)$  in a strip can be tuned *in situ* by control wires which can produce an inverted  $J(x)$  profile with controllable dips at the edges to mitigate current crowding at lithographic defects and block premature penetration of vortices. This approach offers a principal opportunity to overcome the Pearl limit in developing *straight and wide* superconducting strip single photon detectors without the need of meandering SNSPDs to increase the active photon-sensitive area. Furthermore, a "flat noodle" periodic array of such straight strip detectors like those shown in Fig. 7 can be used for the development of multi-pixel cameras beyond the current state-of-the-art<sup>69</sup>. Here each strip can be integrated with either side control wires shown in Fig. 2 or a thin film control underlayer shown in Figs. 5 and 9, respectively. An array of bilayers tuned by its own return current shown in Fig. 7 does not require separate current sources for the underlayers and practically eliminate the Pearl current crowding in strips of any width, but do not provide controllable dips in  $J(x)$  at the edges. The latter can be achieved in a strip integrated with either side controlled wires or a control underlayer fed by separate current sources, as shown in Figs. 2 and 9.

The control wires can be used to tune resistive states caused by the motion of vortices. For instance, strips integrated with control wires have non-reciprocal current-voltage characteristics and can be used for the development of superconducting diodes which switch to highly resistive state above different critical currents  $I_c^+$  and  $I_c^-$  depending on their polarity relative to  $I_1$ . In turn, tuning the dips in  $J(x)$  at the edges of a strip can give rise to a continuous transition from the resistance dominated by penetration of vortices from the edges to the resistance dominated by unbinding of VAV pairs. This happens as the current in control wires exceeds a sample-dependent threshold  $I_1 > I_1^*$  at which an abrupt increase in the logarithmic slope of thermally-activated dark count rate  $d \ln S/dI$  or voltage  $d \ln V/dI$  occurs in the subcritical re-

gion of  $I < I_c^+$  or  $I < I_c^-$ . This behavior of  $S(I, I_1)$  was observed on WSi SNSPD with Nb control wires <sup>38</sup>.

The resistive state at  $I_1 > I_1^*$  is determined by the bulk VAV pair unbinding <sup>36,37</sup>, so the measurements of the voltage-current characteristics  $V(I, T)$  of a strip with control wires can probe the Berezinskii-Kosterlitz-Thouless physics not masked by penetration of single vortices from the edges. Such detectors can be a unique testbed for the investigation of the extreme dynamics of superfast vortices, like those in superconducting resonator cavities <sup>70</sup>. As far as SNSPDs are concerned, they can be tuned by control wires to their ultimate sensitivity limit because the dark counts caused by penetration of vortices from the edges is blocked and detectors operate at the highest bias current given by Eq. (36), where the operational  $S_c$  is only limited by the VAV pair unbinding. This state has the highest photon sensitivity which can benefit many demanding applications mentioned in the Introduction. As follows from Eq. (37), the optimal performance of SNSPD operating at a temperature  $T_1$  can be achieved in SNSPD operating at  $T_2 > T_1$  with the same  $S_c$  and the depairing current fraction  $I_{c2}/I_d$  using the materials for which

$$T_1 \Lambda_1(T_1) = T_2 \Lambda_2(T_2). \quad (38)$$

Besides the fundamental limits of  $I_{c2}$  and the photon sensitivity determined by the VAV pair unbinding, there are also technological and materials science limitations of the SNSPD performance operating at  $I \simeq I_d$ . Once the width limits imposed by the Pearl screening the lithographic defects are lifted by control wires, the SNSPD performance can be limited by inhomogeneities of superconducting properties due to materials defects, local non-stoichiometry, film adhesion with the substrate, etc. Particularly grain boundaries in polycrystalline films can impede current and cause transformation of ultra-fast vortices into phase slips or VAV pairs <sup>71</sup> at  $I \ll I_d$ . The current-blocking grain boundaries are characteristic of materials with short coherence length like NbN, Nb<sub>3</sub>Sn, or superconducting pnictides or cuprates <sup>72</sup>, so operating SNSPDs near the depairing limit is facilitated in amorphous superconductors like WSi <sup>42</sup>.

## ACKNOWLEDGMENTS

This work was supported by DARPA SynQuaNon Program under grant HR0011-24-2-0386. I am grateful to Adam McCaughan, Marti Stevens, Kristen Parzuchowski, and Eli Mueller of NIST for many illuminating discussions and a very productive collaboration.

## Appendix A: Numerical solution of Eqs. (5) and (6).

Equations (5) and (6) were solved by discretizing  $u_n = s(n-1)$ ,  $n = 1, \dots, N_1$  and introducing a vector  $Q_n =$

$(Q_1, Q_2, \dots, Q_{N_1})$  which includes  $Q(sn)$  at  $1 < n < N$  and  $Q_1(sn)$  at  $N+1 < n < N_1$  with  $s = 1/(N-1)$ ,  $N_1 = [(1+l)N]$  and  $N = 4 \cdot 10^3$ . As a result, Eqs. (5) and (6) take the matrix form:

$$\sum_m M_{nm} Q_m = \alpha_n, \quad Q_n = \sum_m M_{nm}^{-1} \alpha_m. \quad (A1)$$

Here  $M_{nm}$  is given below,  $\alpha_n = \alpha$  at  $1 < n < N$ ,  $\alpha_n = \beta$  at  $N+1 < n < N_1$ . To express  $\alpha$  and  $\beta$  in terms of currents  $I = (4s/\mu_0 \Lambda) \sum_{n=1}^N Q_n$  and  $I_1 = (2s/\mu_0 \Lambda_1) \sum_{n=N+1}^{N_1} Q_n$ , we sum up the second Eq. (A1) over  $n$  using that  $\alpha_m$  are constants at  $1 < m < N$  and  $N+1 < m < N_1$ . This yields:

$$I = A_0 \alpha + B_0 \beta, \quad I_1 = A_1 \beta + B_1 \alpha, \quad (A2)$$

Hence,

$$\alpha = \frac{A_1 I - B_0 I_1}{A_0 A_1 - B_0 B_1}, \quad \beta = \frac{A_0 I_1 - B_1 I}{A_0 A_1 - B_0 B_1}, \quad (A3)$$

where

$$A_0 = \frac{4s}{\mu_0 \Lambda} \sum_{n=0}^N \sum_{m=0}^N M_{nm}^{-1}, \quad (A4)$$

$$B_0 = \frac{4s}{\mu_0 \Lambda} \sum_{n=0}^N \sum_{m=N+1}^{N_1} M_{nm}^{-1}, \quad (A5)$$

$$A_1 = \frac{2s}{\mu_0 \Lambda_1} \sum_{n=N+1}^{N_1} \sum_{m=N+1}^{N_1} M_{nm}^{-1}, \quad (A6)$$

$$B_1 = \frac{2s}{\mu_0 \Lambda_1} \sum_{n=0}^N \sum_{m=N+1}^{N_1} M_{nm}^{-1} \quad (A7)$$

The matrix elements  $M_{nm}$  are given by

$$M_{nm} = \delta_{nm} - 2ks \ln |(n^2 - m^2)s^2|, \quad (A8)$$

$$0 < n < N, \quad 1 < m < N;$$

$$M_{nm} = -k_1 s \ln[((m^2 - n^2)s^2 + h^2)^2 + (2hns)^2], \quad (A9)$$

$$0 < n < N, \quad N+1 < m < N_1;$$

$$M_{nm} = -ks \ln[((m^2 - n^2)s^2 + h^2)^2 + (2hns)^2], \quad (A10)$$

$$N+1 < n < N_1, \quad 1 < m < N;$$

$$M_{nm} = \delta_{nm} - 2k_1 s \ln |(n^2 - m^2)s^2|, \quad (A11)$$

$$N+1 < n < N_1, \quad N+1 < m < N_1.$$

## Appendix B: Energy of the Pearl vortex in a strip

The energy of a vortex  $E(u)$  in a strip is a work against the Lorentz force of local current density at the vortex core as the vortex moves from the edge of the strip at  $x = 0$  to  $x = u$ :

$$E(u) = -\phi_0 \int_0^u \tilde{J}(x) dx \quad (B1)$$

In the London theory the driving current density at the vortex core  $\tilde{J}(x) = J_i(x) + J(x)$  is a sum of the transport  $J(x)$  and  $J_i(x)$  induced by the edges. Here  $J_i(x, u)$  is calculated by the method of images, as shown in Fig. 22:

$$J_i = \sum_{n=-\infty}^{\infty}' J_v(x-2wn-u) - \sum_{n=-\infty}^{\infty} J_v(x-2nw+u), \quad (\text{B2})$$

where  $J_v(x-u)$  is the y-component of the current density produced by the Pearl vortex in an infinite film<sup>32</sup>, the first and the second sums in Eq. (B2) describes contributions of all image vortices and antivortices, respectively, and the prime means that the term with  $n = 0$  is excluded.

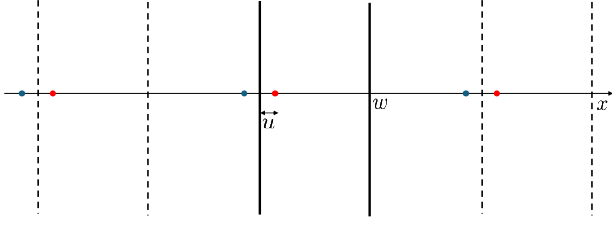


FIG. 22. Image vortices (red) and antivortices (blue) ensuring the boundary conditions  $J_x(0) = J_x(w) = 0$  for a vortex spaced by  $u$  from the edge of a strip of width  $w$ .

Setting  $x = u$  and writing Eq. (B2) in the Fourier space yields:

$$J_i(u) = \frac{2\phi_0}{\mu_0} \int \frac{d^2k}{(2\pi)^2} \frac{ik_x}{k(1+\Lambda k)} \times \left[ e^{2ik_x u} \sum_n e^{-2ik_x w n} - \sum_n' e^{-2ik_x w n} \right], \quad (\text{B3})$$

where the Fourier image  $J_y(\mathbf{k}) = 2i\phi_0 k_x / \mu_0 k(1 + \Lambda k)$  with  $k^2 = k_x^2 + k_y^2$  for the Pearl vortex<sup>32,33</sup> is used. The first sum in the brackets of Eq. (B3) equals  $(\pi/w) \sum_G \delta(k_x + G)$  with  $G = \pi n/w$  and  $n = 0, \pm 1, \pm 2, \dots$ . The second sum in the brackets does not contribute to  $J_i(x)$  after integration over  $k_x$  as all forces acting on the vortex in the strip from the image vortices cancel each other, whereas forces from the image antivortices do not (see Fig. 22). Hence,

$$J_i(u) = \frac{\phi_0}{\pi\mu_0 w} \sum_G \int_0^\infty \frac{G \sin(2Gu) dk_y}{\sqrt{G^2 + k_y^2(1 + \Lambda\sqrt{G^2 + k_y^2})}} \quad (\text{B4})$$

The substitution  $k_y = G \tan t$  reduces the integral  $I_0$  in Eq. (B4) to:

$$I_0 = \int_0^{\pi/2} \frac{G dt}{G\Lambda + \cos t} = \frac{2G}{\sqrt{(G\Lambda)^2 - 1}} \tan^{-1} \left[ \frac{G\Lambda - 1}{G\Lambda + 1} \right]^{1/2}. \quad (\text{B5})$$

A real form of  $I_0$  is:

$$I_0 = \frac{G \cos^{-1}(1/G\Lambda)}{\sqrt{(G\Lambda)^2 - 1}}, \quad G\Lambda > 1 \quad (\text{B6})$$

$$I_0 = \frac{G}{\sqrt{1 - (G\Lambda)^2}} \ln \frac{1 + \sqrt{1 - (G\Lambda)^2}}{G\Lambda}, \quad G\Lambda < 1 \quad (\text{B7})$$

As a result, Eq. (B1) becomes:

$$E(u) = E_v(u) - \frac{2\phi_0}{\mu_0\Lambda} \int_0^u Q(x) dx, \quad (\text{B8})$$

$$E_v(u) = \sum_{n=1}^N E_n \sin^2(\pi n u / w), \quad (\text{B9})$$

$$E_n = \frac{4\epsilon \cos^{-1}(p/n)}{\pi \sqrt{n^2 - p^2}}, \quad n > p \quad (\text{B10})$$

$$E_n = \frac{4\epsilon}{\pi \sqrt{p^2 - n^2}} \ln \frac{p + \sqrt{p^2 - n^2}}{n}, \quad n < p \quad (\text{B11})$$

where  $p = w/\pi\Lambda$ ,  $\epsilon = \phi_0^2/2\pi\mu_0\Lambda$  and the cutoff  $N \sim w/\xi \gg 1$  is evaluated below. For a narrow strip  $w \ll \pi\Lambda$ , Eqs. (B9) and (B10) simplify to:

$$E_v = \epsilon \sum_{n=1}^N \frac{1}{n} \left[ 1 - \cos \frac{2\pi n u}{w} \right] = \epsilon \left[ \ln N + \gamma + \ln \left( 2 \sin \frac{\pi u}{w} \right) \right], \quad (\text{B12})$$

where  $\gamma = 0.577$  is the Euler constant. The cutoff  $N = [0.94w/\xi] \gg 1$  accounts for the finite core size and the energy of the vortex core  $\epsilon_0$  to be added to Eq. (B12):

$$E_v = \epsilon \ln \left[ \frac{2w}{\pi\xi} \left( \sin \frac{\pi u}{w} \right) \right] + \epsilon_0 \quad (\text{B13})$$

Here  $\epsilon_0 = 0.38\epsilon$  was obtained from the GL numerical calculations of  $H_{c1}$ <sup>53</sup> and simulations of a vortex in a strip<sup>56</sup>. Equation (B13) can be written in the form<sup>52</sup>

$$E_v = \epsilon \ln \left[ \frac{w}{\pi\tilde{\xi}} \sin \left( \frac{\pi u}{w} \right) \right], \quad (\text{B14})$$

where  $\tilde{\xi} = 0.34\xi$  and  $0.34 = 0.5 \exp(-0.38)$  absorbs the numerical factors, so that  $E_v(u) \rightarrow 0$  at  $u = \tilde{\xi} \ll w$ . To improve convergence of the series, Eq. (B14) was added and subtracted from Eq. (B9), giving Eq. (17).

\* gurevich@odu.edu

<sup>1</sup> J. Zmuidzinas. Superconducting microresonators: physics and applications. *Annu. Rev. Cond. Mat. Phys.* **3**, 169–214 (2012).

<sup>2</sup> A. Blais, A. L. Grimsom, S. M. Girvin, and A. Wallraff. Circuit quantum electrodynamics. *Rev. Mod. Phys.* **93**, 025005 (2021).

<sup>3</sup> G. N. Gol'tsman, O. Okunev, G. Chulkova, A. Lipatov, A. Semenov, K. Smirnov, B. Voronov, A. Dzardanov, C. Williams, and R. Sobolewski. Picosecond superconducting single-photon optical detector. *Appl. Phys. Lett.* **79**, 705 (2001).

<sup>4</sup> I. E. Zadeh, J. Chang, J. W. N. Los, S. Gyger, A. W. Elshaari, S. Steinhauer, S. N. Dorenbos, and V. Zwiller. Superconducting nanowire single-photon detectors: A perspective on evolution, state-of-the-art, future developments, and applications. *Appl. Phys. Lett.* **118**, 190502 (2021).

<sup>5</sup> F. P. Venzaa and M. Colangeloa. Research trends in single-photon detectors based on superconducting wires. *APL Photon.* **10**, 040901 (2025).

<sup>6</sup> H. Takesue, S. W. Nam, Q. Zhang, R. H. Hadfield, T. Honjo, K. Tamaki, and Y. Yamamoto, Quantum key distribution over a 40-dB channel loss using superconducting single-photon detectors. *Nature Photon.* **1**, 343 (2007).

<sup>7</sup> Y. Liu, W.-J. Zhang, C. Jiang, J.-P. Chen, C. Zhang, W.-X. Pan, D. Ma, H. Dong, J.-M. Xiong, C.-J. Zhang, H. Li, R.-C. Wang, J. Wu, T.-Y. Chen, L. You, X.-B. Wang, Q. Zhang, J.-W. Pan, Experimental twin-field quantum key distribution over 1000 km fiber distance. *Phys. Rev. Lett.* **130**, 210801 (2023).

<sup>8</sup> H. Takesue, S. D. Dyer, M. J. Stevens, V. Verma, R. P. Mirin, S. W. Nam, Quantum teleportation over 100 km of fiber using highly efficient superconducting nanowire single-photon detectors. *Optica* **2**, 832 (2015).

<sup>9</sup> H. Shibata, T. Honjo, K. Shimizu. Quantum key distribution over a 72 dB channel loss using ultralow dark count superconducting single-photon detectors. *Opt. Lett.* **39**, 5078 (2014).

<sup>10</sup> R. Valivarthi, M. G. Puigibert, Q. Zhou, G. H. Aguilar, V. B. Verma, F. Marsili, M. D. Shaw, S. W. Nam, D. Oblak, W. Tittel. Quantum teleportation across a metropolitan fibre network. *Nature Photon.* **10**, 676 (2016).

<sup>11</sup> H. Takesue, S. D. Dyer, M. J. Stevens, V. Verma, R. P. Mirin, and S. W. Nam. Quantum teleportation over 100 km of fiber using highly efficient superconducting nanowire single-photon detectors. *Optica* **2**, 832 (2015).

<sup>12</sup> R. Valivarthi *et al.* Teleportation system toward a quantum internet. *Phys. Rev. X Quantum* **1**, 020317 (2020).

<sup>13</sup> F. Najafi, J. Mower, N. C. Harris, F. Bellei, A. Dane, C. Lee, X. Hu, P. Kharel, F. Marsili, S. Assefa, K. K. Berggren, and D. Englund. On-chip detection of non-classical light by scalable integration of single-photon detectors. *Nature Commun.* **6**, 5873 (2015).

<sup>14</sup> A. N. McCaughan, E. Toomey, M. Schneider, K. K. Berggren, and S. W. Nam. A kinetic-inductance-based superconducting memory element with shunting and sub-nanosecond write times. *Supercond. Sci. Technol.* **32** 015005 (2018).

<sup>15</sup> E. E. Wollman, V. B. Verma, A. B. Walter, J. Chiles, B. Korzh, J. P. Allmaras, Y. Zhai, A. E. Lita, A. N. McCaughan, E. Schmidt, S. Frasca, R. P. Mirin, S. W. Nam, and M. D. Shaw. Recent advances in superconducting nanowire single-photon detector technology for exoplanet transit spectroscopy in the mid-infrared. *J. Astron. Telesc. Instrum. Syst.* **7**, 011004 (2021).

<sup>16</sup> T. Polakovic, W. Armstrong, G. Karapetrov, Z. E. Meziani, and V. Novosad. Unconventional applications of superconducting nanowire single photon detectors. *Nanomaterials* **10**, 1198 (2020).

<sup>17</sup> Y. Hochberg, I. Charaev, S.-W. Nam, V. Verma, M. Colangelo, and K. K. Berggren. Detecting sub-GeV dark matter with superconducting nanowires. *Phys. Rev. Lett.* **123**, 151802 (2019).

<sup>18</sup> J. Chiles, I. Charaev, R. Lasenby, M. Baryakhtar, J. Huang, A. Roshko, G. Burton, M. Colangelo, K. Van Tilburg, A. Arvanitaki, S. W. Nam, and K. K. Berggren. New constraints on dark photon dark matter with superconducting nanowire detectors in an optical haloscope. *Phys. Rev. Lett.* **128**, 231802 (2022).

<sup>19</sup> F. Xia, M. Gevers, A. Fognini, A. T. Mok, B. Li, N. Akbari, I. E. Zadeh, J. Qin-Dregely, and C. Xu. Short-wave infrared confocal fluorescence imaging of deep mouse brain with a superconducting nanowire single-photon detector. *ACS Photonics* **8**, 2800 (2021).

<sup>20</sup> A. Tamimi, M. Calderola, S. Hambura, J. C. Boffi, N. Noordzij, J. W. N. Los, A. Guardiani, H. Kooiman, L. Wang, C. Kieser, F. Braun, A. Fognini, and R. Prevedel. Deep mouse brain two-photon near-infrared fluorescence imaging using a superconducting nanowire single-photon detector array. *ACS Photonics* **11**, 3960 (2024).

<sup>21</sup> Q. Wang, M. Pan, L. Kreiss, S. Samaei, S. A. Carp, J. D. Johansson, Y. Zhang, M. Wu, R. Horstmeyer, M. Diop, and D. Day-Uei Lia. A comprehensive overview of diffuse correlation spectroscopy: theoretical framework, recent advances in hardware, analysis, and applications. *NeuroImage* **298**, 120793 2024.

<sup>22</sup> D. Yu. Vodolazov. Single-photon detection by a dirty current-carrying superconducting strip based on the kinetic-equation approach. *Phys. Rev. Appl.* **7**, 034014 (2017).

<sup>23</sup> J. R. Clem and K. K. Berggren. Geometry-dependent critical currents in superconducting nanocircuits. *Phys. Rev. B* **84**, 174510 (2011).

<sup>24</sup> A.V. Silhanek, L. Jiang, C. Xue, and B. Vanderheyden. Impact of border defects on the magnetic flux penetration in superconducting films. *Appl. Phys. Rev.* **12**, 041324 (2025).

<sup>25</sup> M. Friesen and A. Gurevich. Nonlinear current flow in superconductors with restricted geometries. *Phys. Rev. B* **63**, 064521 (2001).

<sup>26</sup> L. Embon, Y. Anahory, Z. L. Jelic, E. O. Lachman, Y. Myasoedov, M. E. Huber, G. P. Mikitik, A. V. Silhanek, M. V. Milosevic, A. Gurevich, and E. Zeldov. Imaging of super-fast dynamics and flow instabilities of superconducting vortices. *Nature Commun.* **8**, 85 (2017).

<sup>27</sup> O. V. Dobrovolskiy, D. Yu Vodolazov, F. Porrati, R. Sachser, V. M. Bevz, M. Yu Mikhailov, A. V. Chumak, and M. Huth. The ultra-fast dynamics of superconducting vortices *Nature Commun.* **11** 3291 (2020).

<sup>28</sup> A. I. Bezuglyj, V. A. Shklovskij, B. Budinská, B. Eichner, V. M. Bevz, M. Yu. Mikhailov, D. Yu. Vodolazov, W. Lang,

and O. V. Dobrovolskiy. Vortex jets generated by edge defects in current-carrying superconductor thin strips. *Phys. Rev. B* **105**, 214507 (2022).

<sup>29</sup> P. Leiderer, J. Boneberg, P. Brüll, V. Bujok, and S. Herminghaus. Nucleation and growth of a flux instability in superconducting  $\text{YBa}_2\text{Cu}_3\text{O}_{7-x}$  films. *Phys. Rev. Lett.* **71**, 2646 (1993).

<sup>30</sup> I. S. Aranson, A. Gurevich, M. S. Welling, R. J. Wijngaarden, V. K. Vlasko-Vlasov, V. M. Vinokur, and U. Welp. Dendritic flux avalanches and nonlocal electrodynamics in thin superconducting films. *Phys. Rev. Lett.* **94**, 037002 (2005).

<sup>31</sup> P. Mikheenko, T. H. Johansen, S. Chaudhuri, I. J. Maasalta, and Yu. M. Galperin. Ray optics behavior of flux avalanche propagation in superconducting films. *Phys. Rev. B* **91**, 060507 (2015).

<sup>32</sup> J. Pearl. Current distribution in superconducting films carrying quantized fluxons. *Appl. Phys. Lett.* **5**, 65 (1964).

<sup>33</sup> P.G. de-Gennes. *Superconductivity of Metals and Alloys*. Benjamin, New York-Amsterdam, 1966.

<sup>34</sup> M. Yabuno, F. China, H. Terai, Hirotaka, and S. Miki. Superconducting wide strip photon detector with high critical current bank structure. *Optica Quantum* **1**, 26 (2023).

<sup>35</sup> S. Strohauer, F. Wietschorke, C. Schmid, S. Grotowski, L. Zugliani, B. Jonas, K. Müller, and J. J. Finley. Current crowding-free superconducting nanowire single-photon detectors. *Sci. Adv.* **11**, ead0502 (2025).

<sup>36</sup> B. I. Halperin and D. R. Nelson. Resistive transition in superconducting films. *J. Low Temp. Phys.* **36**, 599 (1979).

<sup>37</sup> P. Minnhagen. The two-dimensional Coulomb gas, vortex unbinding, and superfluid-superconducting films. *Rev. Mod. Phys.* **59**, 1001 (1987).

<sup>38</sup> K. M. Parzuchowski, E. Mueller, B. G. Oripov, B. Hampsel, R. A. Chowdhury, S. Patel, D. Kuznesof, E. K. Batson, V. B. Verma, J. P. Allmaras, M. J. Stevens, A. Gurevich, and A. N. McCaughan. Approaching the intrinsic performance limits of superconducting strip photon detectors up to 0.1 mm wide. arXiv:2601.15971.

<sup>39</sup> A. E. Brenneman. The in-line cryotron. *Proc. IEEE*, **51**, 442 (1963).

<sup>40</sup> P. S. Swartz and H. R. Hart, Jr. Asymmetries of the critical surface current in type-II superconductors. *Phys. Rev.* **156**, 412 (1967).

<sup>41</sup> V. L. Newhouse. Superconducting Devices. In *Superconductivity*. Ed. R. D. Parks, Marcel Dekker Inc., New York, v. 2, pp. 1283-1342 (1969).

<sup>42</sup> X. Zhang, A. Engel, Q. Wang, A. Schilling, A. Semenov, M. Sidorova, H-W Hübers, I. Charaev, K. Ilin, and M. Siegel. Characteristics of superconducting tungsten silicide  $\text{W}_x\text{S}_{1-x}$  for single photon detection. *Phys. Rev. B* **94**, 174509 (2016).

<sup>43</sup> A. Gurevich and V. M. Vinokur. Phase textures induced by dc current pairbreaking in multilayer structures and two-gap superconductors. *Phys. Rev. Lett.* **97**, 137003 (2006).

<sup>44</sup> Yu. A. Genenko. Overcritical states of a superconductor strip in all-superconducting environments. *Phys. Rev. B* **66**, 184520 (2002).

<sup>45</sup> J. R. Clem. Field and current distribution and ac losses in bifilar stack of superconducting strips. *Phys. Rev. B* **77**, 134506 (2008).

<sup>46</sup> L. R. Cadorim, E. Sardella, and C. C. de Souza Silva. Harnessing the superconducting diode effect through inhomogeneous magnetic fields. *Phys. Rev. Appl.* **21**, 054040 (2024).

<sup>47</sup> M. Nadeem, M. S. Fuhrer, and X. Wang. The superconducting diode effect. *Nature Rev. Phys.* **5**, 558 (2023).

<sup>48</sup> P. J. W. Moll and V. B. Geshkenbein. Evolution of superconducting diodes. *Nature Physics* **19**, 1379 (2023).

<sup>49</sup> J. Ma, R. Zhan, and X. Lin. Superconducting diode effects: mechanisms, materials and applications. *Adv. Physics Res.* **4**, 2400180 (2025).

<sup>50</sup> F. Tafuri, J. R. Kirtley, D. Born, D. Stornaiuolo, P. G. Medaglia, P. Orgiani, G. Balestrino and V. G. Kogan. Dissipation in ultra-thin current-carrying superconducting bridges; evidence for quantum tunneling of Pearl vortices. *Europhys. Lett.* **73**, 948 (2006).

<sup>51</sup> M. Perego, P. Koopmann, C. G. Agero, A. M. Torá, A. O. Denisov, T. Taniguchi, K. Watanabe, V. Geshkenbein, G. Blatter, T. Ihn, and K. Ensslin. Pearl-Vortex Tunneling in Magic-Angle Twisted Graphene. arXiv:2601.21735v1

<sup>52</sup> A. Gurevich and V. M. Vinokur. Size effects in the nonlinear resistance and flux creep in a virtual Berezinskii-Kosterlitz-Thouless state of superconducting films. *Phys. Rev. Lett.* **100**, 227007 (2008).

<sup>53</sup> G. Stejic, A. Gurevich, E. Kadyrov, D. Christen, R. Joynt, and D. C. Larbalestier. Effect of geometry on the critical currents of thin films. *Phys. Rev. B* **49**, 1274 (1994).

<sup>54</sup> K. K. Likharev. The formation of a mixed state in planar superconductor films. *Sov. Radiophys.* **14**, 722 (1972).

<sup>55</sup> V. I. Volkovskii, G. L. Lunts, and I. G. Aramanovich. A Collection of Problems of Complex Analysis. In *International Series of Monographs in Pure and Applied Mathematics*. v. 68, Pergamon, Oxford, 1965.

<sup>56</sup> D. Yu. Vodolazov. Saddle point states in two-dimensional superconducting films biased near the depairing current. *Phys. Rev. B* **85**, 174507 (2012).

<sup>57</sup> N. Nakagawa and V. G. Kogan. Vortex in superconducting thin-film strips of arbitrary width. *Supercond. Sci. Technol.* **37**, 055008 (2024).

<sup>58</sup> J. R. Clem, R. P. Huebener, and D. E. Gallus. Gibbs free-energy barrier against irreversible magnetic flux entry into a superconductor. *J. Low Temp. Phys.* **12**, 449 (1973).

<sup>59</sup> E. Zeldov, A. I. Larkin, V. B. Geshkenbein, M. Konczykowski, D. Majer, B. Khaykovich, V. M. Vinokur, and H. Shtrikman. Geometrical barriers in high-temperature superconductors. *Phys. Rev. Lett.* **73**, 1428 (1994).

<sup>60</sup> P. Hänggi, P. Talkner, and M. Borkovec. Reaction-rate theory: fifty years after Kramers. *Rev. Mod. Phys.* **62**, 251 (1990).

<sup>61</sup> H. Bartolf, A. Engel, A. Schilling, K. Il'in, M. Siegel, H.-W. Hübers, and A. Semenov. Current-assisted thermally activated flux liberation in ultrathin nanopatterned NbN superconducting meander structures. *Phys. Rev. B* **81**, 024502 (2010).

<sup>62</sup> J. R. Clem and V. G. Kogan. Kinetic impedance and depairing in thin and narrow superconducting films. *Phys. Rev. B* **86**, 174521 (2012).

<sup>63</sup> E. J. Nicol and J. P. Carbotte. Temperature dependence of the critical pair-breaking current in thin-film, strong-coupling superconductors. *Phys. Rev. B* **43**, 10210 (1991).

<sup>64</sup> A. Sheikhzada and A. Gurevich. Maximum dynamic pair-breaking current and superfluid velocity in nonequilibrium superconductors. *Phys. Rev. B* **102**, 104507 (2020).

<sup>65</sup> J. P. Allmaras, A. G. Kozorezov, M. Colangelo, B. A. Korzh, M. D. Shaw, and K. K. Berggren. Effect of temperature fluctuations on kinetic inductance and depairing in thin and narrow superconducting nanowire detectors. *Phys. Rev. B* **107**, 104520 (2023).

<sup>66</sup> J. Makita, C. Sundahl, G. Ciovati, C. B. Eom, and A. Gurevich. Nonlinear Meissner effect in  $\text{Nb}_3\text{Sn}$  coplanar resonators. *Phys. Rev. Research* **4**, 013156 (2022).

<sup>67</sup> T. Kubo. Superfluid flow in disordered superconductors with Dynes pair-breaking scattering: Depairing current, kinetic inductance, and superheating field. *Phys. Rev. Research* **2**, 033203 (2020).

<sup>68</sup> J. Zasadzinski. Tunneling spectroscopy of conventional and unconventional superconductors. In *The Physics of Superconductors*, Ed. K. H. Bennemann and J. B. Ketterson, New York: Springer-Verlag, v. 1, pp. 591-643 (2004).

<sup>69</sup> B. G. Oripov, D. S. Rampini, J. Allmaras, M. D. Shaw, S. W. Nam, B. Korzh, and A. N. McCaughan. A superconducting nanowire single-photon camera with 400,000 pixels. *Nature* **622**, 730 (2023).

<sup>70</sup> A. Gurevich. Tuning microwave losses in superconducting resonators. *Supercond. Sci. Technol.* **36**, 063002 (2023).

<sup>71</sup> A. Sheikhhada and A. Gurevich. Dynamic transition of vortices into phase slips and generation of vortex-antivortex pairs in thin film Josephson junctions under dc and ac currents. *Phys. Rev. B* **95**, 214507 (2017).

<sup>72</sup> J.H. Durrell, C.B. Eom, A. Gurevich, E.E. Hellstrom, C. Tarantini, A. Yamamoto, and D.C. Larbalestier. The behavior of grain boundaries in the Fe-based superconductors. *Rep. Prog. Phys.* **74**, 124511 (2011).